

Far-Ultraviolet Spectra of Main-Sequence O Stars at Extremely Low Metallicity

O. GRACE TELFORD,¹ JOHN CHISHOLM,² KRISTEN B. W. MCQUINN,¹ AND DANIELLE A. BERG²

¹*Rutgers University, Department of Physics and Astronomy, 136 Frelinghuysen Road, Piscataway, NJ 08854, USA*

²*Department of Astronomy, The University of Texas at Austin, 2515 Speedway, Stop C1400, Austin, TX 78712-1205, USA*

ABSTRACT

Metal-poor massive stars dominate the light we observe from star-forming dwarf galaxies and may have produced the bulk of energetic photons that reionized the universe at high redshift. Yet, the rarity of observations of individual O stars below the 20% solar metallicity (Z_{\odot}) of the Small Magellanic Cloud (SMC) hampers our ability to model the ionizing fluxes of metal-poor stellar populations. We present new *Hubble Space Telescope* far-ultraviolet (FUV) spectra of three O-dwarf stars in the galaxies Leo P (3% Z_{\odot}), Sextans A (6% Z_{\odot}), and WLM (14% Z_{\odot}). We quantify equivalent widths of photospheric metal lines and strengths of wind-sensitive features, confirming that both correlate with metallicity. We infer the stars' fundamental properties by modeling their FUV through near-infrared spectral energy distributions and identify stars in the SMC with similar properties to each of our targets. Comparing to the FUV spectra of the SMC analogs suggests that (1) the star in WLM has an SMC-like metallicity, and (2) the most metal-poor star in Leo P is driving a much weaker stellar wind than its SMC counterparts. We measure projected rotation speeds and find that the two most metal-poor stars have high $v \sin(i) \geq 290 \text{ km s}^{-1}$, and estimate just a 3–6% probability of finding two fast rotators if the metal-poor stars are drawn from the same $v \sin(i)$ distribution observed for O dwarfs in the SMC. These observations suggest that models should include the impact of rotation and weak winds on ionizing flux to accurately interpret observations of metal-poor galaxies in both the near and distant universe.

1. INTRODUCTION

1.1. *Uncertainties in Modeling Metal-Poor Massive Stellar Populations*

Massive stars dominate the spectral energy distributions (SEDs) of star-forming galaxies. Throughout their lives and during their explosive deaths as supernovae, they deposit energy, momentum, and ionizing photons into the surrounding interstellar medium (ISM). This feedback from massive stellar populations is widely recognized as an important regulator of star formation and galaxy evolution processes (e.g., Somerville & Davé 2015; Naab & Ostriker 2017). Bursts of star formation can efficiently create low-density channels in the ISM through which ionizing photons produced by young, massive stars can escape, particularly from low-mass galaxies in the early universe (e.g., Wise & Cen 2009; Trebitsch et al. 2017). Thus, massive stars in metal-poor dwarf galaxies are likely drivers of the reionization of the universe at high redshift, $z \gtrsim 6$ (Ouchi et al. 2009;

Robertson et al. 2015; Finkelstein et al. 2019), but their ionizing fluxes remain uncertain.

The neutral intergalactic medium is opaque to H-ionizing photons ($\lambda \leq 912 \text{ \AA}$) during the epoch of reionization (e.g., Becker et al. 2001). Observations of high- z galaxies at longer rest wavelengths must therefore be modeled with stellar population synthesis (SPS) codes to infer the ionizing flux from massive stars. SPS models combine template stellar spectra, stellar evolution models, an initial mass function (IMF), and a star formation history (SFH) parameterization to predict the intrinsic SED of a stellar population (Tinsley 1980; Conroy 2013). From this, the ionizing flux from massive stars can be inferred, then combined with observational constraints on ionizing photon escape fractions (e.g., Izotov et al. 2016; Steidel et al. 2018) and the galaxy luminosity function at high z (e.g., Livermore et al. 2017; Oesch et al. 2018) to predict the total ionizing photons escaping from the predominantly metal-poor galaxies in the early universe. Our understanding of the contribution of galaxies to cosmic reionization is therefore highly sensitive to the stellar evolution models and theoretical spectra adopted in SPS codes.

At solar metallicity (Z_{\odot}), a large population of massive stars in the Milky Way has been spectroscopically observed and forms a useful benchmark for calibrating stellar models (e.g., Howarth & Prinja 1989; Walborn & Fitzpatrick 1990; Przybilla et al. 2010). The nearest star-forming dwarf galaxies that host sub- Z_{\odot} massive stars, the Large Magellanic Cloud (LMC; 50% Z_{\odot}) and Small Magellanic Cloud (SMC; 20% Z_{\odot} ; Dufour 1984), have been used to test the predictions of stellar models over a range of metallicity (Z ; e.g., Mokiem et al. 2007; Dorn-Wallenstein & Levesque 2020), but few spectroscopic observations of more metal-poor massive stars exist due to their large distances. Even individual stars in “nearby” dwarf irregular galaxies just outside the Local Group are very faint and therefore expensive to observe, leaving us with few empirical constraints on stellar models appropriate to interpret observations of metal-poor galaxies in the early universe.

There is evidence from nearby metal-poor galaxies that stellar models are incomplete at low Z . SPS models combined with high-quality SFHs inferred from resolved stellar populations of dwarf galaxies predict an excess of far-ultraviolet (FUV) flux over what is observed, even when the near-ultraviolet (NUV) flux is matched well (McQuinn et al. 2015a). In vigorously star-forming metal-poor galaxies, extreme nebular emission lines with strengths comparable to those observed in high- z galaxies cannot be explained by the ionizing fluxes predicted by SPS models fit to the integrated light from the massive stellar populations (e.g., Berg et al. 2018, 2019; Senchyna et al. 2019). A variety of possible solutions have been proposed, including binary interactions, a top-heavy IMF, and problems with theoretical spectra and/or evolution models at low Z (e.g., McQuinn et al. 2015a; Kehrig et al. 2018; Götberg et al. 2019; Senchyna et al. 2021), but current observations cannot distinguish among these possibilities. Empirical constraints on the SEDs and evolution of low- Z massive stars are required to identify the cause of these model discrepancies and improve our ability to model metal-poor galaxies, both nearby and at high z .

1.2. Constraints on the Astrophysics of Massive Stars from FUV Spectroscopy

Predictions of stellar evolution models depend sensitively on the initial rotation speeds and prescriptions for mass-loss rates (\dot{M}_{\star}) via stellar winds that they adopt. Both affect the time evolution of massive stars’ surface properties and their main-sequence lifetimes, which in turn set the total number of ionizing photons that a stellar population is predicted to produce (e.g., Levesque et al. 2012; Smith 2014). Theoretical grids of hot stel-

lar spectra calculated with atmosphere modeling codes predict the metal opacities, wind line strengths, and ionizing fluxes of massive stars (e.g., Lanz & Hubeny 2003; Eldridge et al. 2017; Martins & Palacios 2021). Below 20% Z_{\odot} , these assumptions and predictions remain unconstrained by observations, so new measurements of the stellar and wind properties of individual OB stars are needed.

FUV spectroscopy is a particularly important tool for measuring the properties of OB stars, as this spectral region contains many transitions of highly ionized metals and falls close to the peak of hot stellar SEDs. The same metals, particularly Fe, that remove flux in the FUV also absorb strongly in the ionizing extreme UV part of the spectrum, so the observed opacities of metal lines in the FUV provide important constraints on the ionizing photon production by massive stars. Metal lines absorb the emergent flux from hot stars to accelerate the expanding wind, forming P-Cygni profiles in the FUV that provide sensitive diagnostics of the terminal velocity (v_{∞}) and \dot{M}_{\star} (Lamers & Cassinelli 1999).

At low Z , line-driven stellar winds are expected to weaken due to reduced metal opacities, though theoretical mass-loss prescriptions differ in the absolute \dot{M}_{\star} for a given set of stellar parameters and predict somewhat different scalings with Z (e.g., Vink et al. 2001; Bestenlehner 2020; Björklund et al. 2021; Vink & Sander 2021). Observations in the Milky Way and Magellanic Clouds support the expectation of decreasing wind strength down to 20% Z_{\odot} (e.g., Mokiem et al. 2007), though some empirical studies have found even weaker winds than expected in the SMC (Bouret et al. 2013; Ramachandran et al. 2019). Measurements of \dot{M}_{\star} and v_{∞} are rare for more metal-poor stars, so the question of whether these wind parameters obey the same scalings down to very low Z remains open (Tramper et al. 2011, 2014; Garcia et al. 2014; Bouret et al. 2015).

Winds can remove angular momentum from stellar surfaces throughout their lifetimes. Since line-driven winds weaken at low Z , metal-poor stars are expected to lose angular momentum less efficiently and thus maintain higher rotation rates throughout their main-sequence lifetimes (e.g., Groh et al. 2019). Observations of many OB stars in the Galaxy, LMC, and SMC hint that typical $v \sin(i)$ increases with decreasing metallicity (e.g., Penny & Gies 2009; Ramachandran et al. 2019). However, only a handful of measurements of $v \sin(i)$ or spectral line broadening have been reported below 20% Z_{\odot} (Tramper et al. 2011, 2014; Garcia et al. 2014; Ramachandran et al. 2021), so it remains unclear whether this trend holds for more metal-poor massive stars. Fortunately, $v \sin(i)$ can be constrained from the

structure of photospheric lines in moderate-resolution FUV spectroscopy (e.g., Penny & Gies 2009; Bouret et al. 2013).

The ongoing *Hubble Space Telescope* (*HST*) Director’s Discretionary Ultraviolet Legacy Library of Young Stars as Essential Standards (ULLYSES) program will measure new high-SNR, medium-to-high resolution ($R \sim 3000 - 45000$) FUV spectra for over 160 OB stars in the LMC and SMC (spanning all luminosity classes for spectral types O2-B1.5, as well as B2-B9 supergiants). These new data will be combined with archival observations to construct a library of FUV spectra for over 230 OB stars, providing an unprecedented benchmark for massive stellar astrophysics down to 20% Z_{\odot} . Yet, ULLYSES will only obtain low-resolution ($R \sim 1500 - 4000$) FUV spectra of 6 OB stars in two more distant and metal-poor galaxies, NGC3109 (18% Z_{\odot} ; Lee et al. 2007) and Sextans A (6% Z_{\odot} ; Skillman et al. 1989). This will significantly add to the dozen published FUV spectra of OB stars in metal-poor dwarf galaxies outside of the Local Group as of this writing (Garcia et al. 2014, 2017; Bouret et al. 2015), but this small sample is not sufficient to benchmark stellar models below 20% Z_{\odot} . Additional spectroscopic observations are needed to test SPS models, which are central to the interpretation of upcoming *James Webb* and *Nancy Grace Roman Space Telescope* observations of high- z galaxies.

Here, we present new FUV spectra of three metal-poor O V stars in the nearby dwarf galaxies Leo P, Sextans A, and WLM (3–14% Z_{\odot}), obtained with the Cosmic Origins Spectrograph (COS) on *HST*. The paper is organized as follows: Section 2 describes the sample of O stars and both spectral and photometric data used in this analysis. Section 3 presents our analysis of the new FUV spectra and SEDs constructed with *HST* photometry, including measurements of photospheric line strengths, wind line strength and velocity extent, projected rotation speed $v \sin(i)$, and constraints on fundamental stellar properties from SED modeling. Section 4 discusses our results in comparison to analog stars in the SMC and implications for modeling metal-poor stellar populations. Section 5 summarizes our conclusions.

We define the terms that we use throughout the paper to refer to two distinct metallicity regimes. First, metal poor or low Z indicates $Z < 20\% Z_{\odot}$, i.e., more metal-poor than the SMC. Second, we use the terms extremely metal poor and very low Z to mean $Z < 10\% Z_{\odot}$ (following the definition of very metal-deficient galaxies by Kunth & Östlin 2000). We also consider the latter category to be substantially more metal-poor than the SMC (by at least a factor of two).

Table 1. Properties of the galaxies hosting the target stars.

Star	Galaxy	$12+\log(\text{O}/\text{H})$ (nebular)	Z/Z_{\odot} (nebular)	Distance (Mpc)
LP26	Leo P	7.17 ± 0.04	0.03	1.62 ± 0.15
S3	Sextans A	7.49 ± 0.04	0.06	1.38 ± 0.05
A15	WLM	7.83 ± 0.06	0.14	0.98 ± 0.04

NOTE—We adopt the star identifiers LP26, S3, and A15 from Evans et al. (2019), Garcia et al. (2019), and Bresolin et al. (2006), respectively. Nebular metallicities for Leo P, Sextans A, and WLM from Skillman et al. (2013), Skillman et al. (1989), and Lee et al. (2005), respectively, are converted to solar units assuming solar abundance ratios and $(12 + \log(\text{O}/\text{H}))_{\odot} = 8.69$ (Asplund et al. 2009). Distances to the galaxies (in the same order) are from McQuinn et al. (2015b), Dalcanton et al. (2009), and Jacobs et al. (2009).

2. OBSERVATIONS AND DATA REDUCTION

In this section, we present the sample of O stars analyzed in this work. We then describe the observations and data reduction for both the new *HST*/COS FUV spectra and the archival *HST* imaging used to measure the broadband photometric properties of the stars.

2.1. The Sample of O V Stars

The goal of this work is to characterize empirically the FUV properties of metal-poor O stars still on the main sequence. We therefore focus on known O stars with luminosity class V (i.e., dwarfs), as these are the least evolved. Only one early-O dwarf in a galaxy more metal-poor than the SMC has ever been analyzed in the FUV, and that star (in IC 1613) appears to have an SMC-like Fe abundance (Bouret et al. 2015). We searched the literature for all spectroscopically confirmed O V stars residing in galaxies with gas-phase abundances below that of the SMC that are close enough that stars can be individually resolved and observed with *HST*/COS (Bresolin et al. 2006; Evans et al. 2019; Garcia et al. 2019). Excluding two stars in Sextans A that will be observed as part of ULLYSES, our final sample consists of the only three known O V stars that matched our metallicity and distance requirements.

Our target stars are LP26 in Leo P (3% Z_{\odot}), S3 in Sextans A (6% Z_{\odot}), and A15 in WLM (14% Z_{\odot}). LP26 is the only known O star in Leo P, which is the closest star-forming galaxy with such low gas-phase metallicity. Host galaxy properties are given in Table 1, and the spectral types and optical magnitudes of the stars are given in Table 2. We use the gas-phase oxygen abundances as estimates of the stellar Z throughout this work, though it is likely that the true metal mass fractions of the stars are different as the α/Fe ratio is known

Table 2. Basic data for the three target stars and *HST*/COS spectra.

Star	Galaxy	RA	Dec.	m_V	A_V	Spectral Type	Exposure Times (s)		Galaxy v_{sys} (km s^{-1})
		(J2000)	(J2000)	(mag)	(mag)		G130M	G160M	
LP26	Leo P	10:21:45.1217	+18:05:16.93	21.51	0.04	O7-8 V	21502	48396	248
S3	Sextans A	10:10:58.1866	-04:43:18.45	20.80	0.09	O9 V	10725	26908	302
A15	WLM	00:02:00.5333	-15:29:52.41	20.25	0.04	O7 V((f))	7880	15698	-115

NOTE—Right ascension is reported in hours, minutes, seconds, and declination is in degrees, arcminutes, arcseconds. Foreground extinction A_V is from Green et al. (2015). Visual magnitudes and spectral types for LP26, S3, and A15 are from McQuinn et al. (2015b), Garcia et al. (2019), and Bresolin et al. (2006), respectively.

to vary across galaxies depending on the recent SFH. Detailed stellar abundance measurements are outside the scope of this work and we defer that analysis to a future paper. All three targets are considered metal-poor, and S3 and LP26 are extremely metal-poor.

2.2. Photometry from Archival *HST* Imaging

We require multi-wavelength photometry that samples the SEDs of the target stars as broadly in wavelength as possible to constrain their fundamental properties (Section 3.4). All of our target stars are covered by high-resolution *HST* imaging in the NUV, optical, and/or near-infrared (NIR), drawn from the programs listed in the caption of Table 3. NUV and NIR images were taken with the Wide-Field Camera 3 (WFC3) UVIS and IR channels, respectively. Optical imaging was taken with the Advanced Camera for Surveys (ACS) Wide Field Camera (WFC) detector for both Leo P and WLM, and with the Wide-Field Planetary Camera 2 (WFPC2) for Sextans A. Both ACS datasets acquired many more images, which reach much fainter magnitudes when combined, than required to reliably measure the bright O star targets. We therefore only use 4 images per filter, taken during the same visit to ensure the best possible alignment. Raw images (*flc.fits, *flt.fits, *c0m.fits, and *c1m.fits files, naming convention depending on the instrument) are retrieved from the Mikulski Archive for Space Telescopes (MAST).

Figure 1 shows optical images of each galaxy hosting one of our target stars in greyscale with the locations of the various *HST* imaging datasets overlaid. The $15' \times 15'$ background images for WLM and Sextans A are taken from the Digitized Sky Survey (DSS). Leo P is smaller and fainter than “classical” dwarf galaxies and is not visible in DSS imaging, so for that galaxy we show an ACS F475W image, approximately $3/4$ on a side. The inset image in shades of purple in each panel shows an example COS acquisition image from our program, discussed further in Section 2.3. Outlines of the various archival *HST* imaging footprints that we use to measure photometry for our target stars are overlaid, with

purple, blue, and red outlines corresponding to NUV, optical, and NIR, respectively.

We perform point spread function (PSF) photometry on the *HST* images using DOLPHOT (Dolphin 2000, 2016). First, we use the tools in DRIZZLEPAC v3.1.8 (Gonzaga et al. 2012) to clean cosmic rays from the images, align the individual images for each galaxy to a common reference frame, and create a deep mosaic in a filter in the middle of the wavelength range spanned by the data (F814W for Sextans A and Leo P, and F475W for WLM). DOLPHOT uses the deep mosaic as a reference to which individual images are aligned and to locate stars. The stars are then photometered in the individual images, and the measurements and uncertainties for each star are combined across all exposures in each filter. Photometry is done simultaneously across all filters for each galaxy. Table 3 reports the measured photometry for each target star in the Vega magnitude system, in which the star Vega is defined to have zero magnitude at all wavelengths, and gives the uncertainties in parentheses below the measurements.

The parameters set in DOLPHOT strongly affect the quality of the resultant photometry. We generally follow the well-tested parameters used by the Panchromatic Hubble Andromeda Treasury (PHAT) survey (Williams et al. 2014, 2021). However, we find that using FITSKY = 2 (which is best for crowded stellar fields) results in our large, bright target stars being divided into multiple sources. Thus, we adopt FITSKY = 3 and the recommended values of RAPER and RPSF for that setting from the instrument-specific DOLPHOT manuals.

In addition to measured flux and uncertainty for each star, DOLPHOT output includes the quality metrics CROWD and SHARP. High CROWD values indicate that the star’s photometry is potentially affected by the presence of nearby sources, while high |SHARP| indicates that the source is more extended than expected for a star (e.g., background galaxy) or too narrow (e.g., cosmic ray). We verify that high-quality photometry is obtained for all three target stars; specifically, $\text{CROWD} \leq 0.45$ mag and $|\text{SHARP}|^2 \leq 0.05$ in all fil-

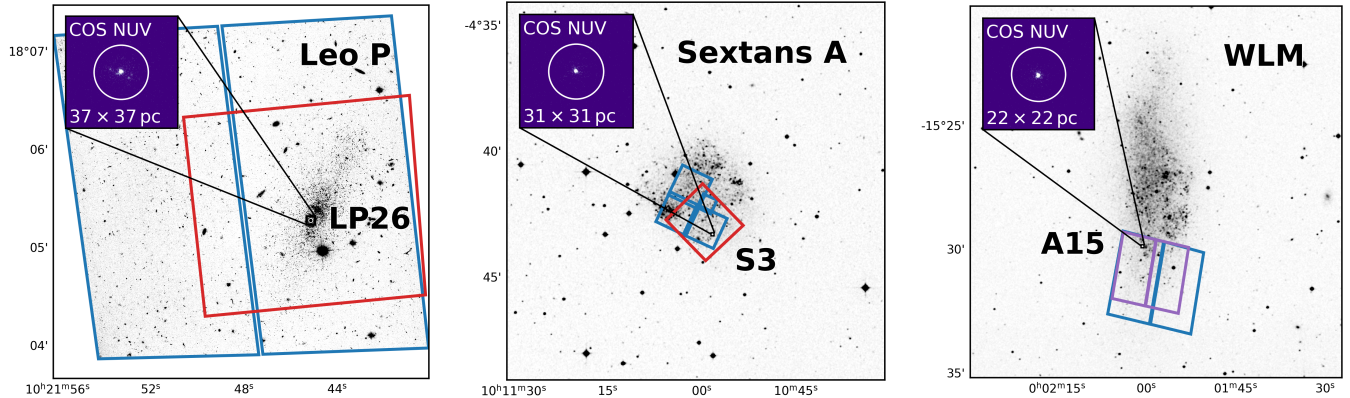


Figure 1. *HST* imaging of the three target O stars in nearby, metal-poor galaxies. From left to right, optical images of Leo P, Sextans A, and WLM are shown in greyscale with a linear stretch, all oriented with north up and east left. The Leo P image is a $3'.4 \times 3'.4$ *HST*/ACS F475W mosaic, while the other two are $15' \times 15'$ DSS images. The purple, blue, and red rectangles show the footprints of the archival *HST* imaging in the NUV, optical, and NIR, respectively, that we use for stellar photometry. The insets centered on the three target stars show cutouts of the COS acquisition images $4''.7$ on a side, with the $2''.5$ -diameter aperture shown as a white circle. Each cutout is annotated with its physical dimensions at the distance of the target star.

Table 3. Photometry measured from archival *HST* imaging.

Star	F275W (mag)	F336W (mag)	F475W (mag)	F555W (mag)	F814W (mag)	F127M (mag)	F139M (mag)	F153M (mag)
LP26	21.513 (0.002)	...	21.929 (0.004)	22.312 (0.064)	22.466 (0.091)	22.341 (0.107)
S3	20.866 (0.005)	21.082 (0.009)	21.492 (0.043)	21.417 (0.036)	21.400 (0.044)
A15	17.788 (0.003)	18.357 (0.002)	20.145 (0.001)	...	20.526 (0.002)

NOTE—Magnitudes are reported in the Vega system, and the uncertainty is given in parentheses below each measurement. These are the raw DOLPHOT outputs and are not corrected for dust extinction. Photometry was measured from *HST* images from the following programs: 13376 (optical; PI: K. McQuinn) and 14845 (NIR; PI: M. Boyer) for LP26; 5915 (optical; PI: E. Skillman) and 14073 (NIR; PI: M. Boyer) for S3; and 15275 (NUV; PI: K. Gilbert) and 13768 (optical; PI: D. Weisz) for A15.

ters. Typical photometric signal-to-noise ratios (SNRs) reach several hundred in the NUV and optical and $\sim 10 - 30$ in the NIR.

We correct the photometric fluxes for Milky Way foreground dust extinction adopting A_V at the location of each star from Green et al. (2015) and a Fitzpatrick (1999) extinction law with $R_V = 3.1$. The shape of the stellar SED affects the magnitude of the extinction correction in each filter. We calculate the corrections for the SED of a 40 kK dwarf to ensure suitability for the O stars in this study.

2.3. *HST*/COS FUV Spectra

We obtained medium-resolution FUV spectra of our targets with *HST*/COS in Cycle 27 over 49 orbits between 2020 April 10–June 16. (GO-15967; PI: J. Chisholm). Table 2 gives basic data for the three

target stars and exposure times of the observations. We used the G130M grating at central wavelength 1291 \AA (FP-POS=3, 4) and the G160M grating at central wavelength 1600 \AA (FP-POS=all). This combination covers many lines that serve as diagnostics of stellar photosphere and wind properties, particularly the C III 1176 \AA and N V 1240 \AA lines in G130M and C IV 1550 \AA in G160M. Observations were taken in TIME-TAG mode using the $2''.5$ Primary Science Aperture (PSA). The calibrated and co-added spectra for all 12 visits (*x1dsum.fits files), processed and extracted with the standard CalCOS pipeline (version 3.3.9), were downloaded from MAST. We verified that the wavelength solutions and flux calibrations using the default parameters were consistent across visits.

Example COS acquisition images for each target star, taken in the NUV channel, are shown in the inset pan-

els of Figure 1. Each inset is a $4.7''$ on a side cutout of the acquisition image, and we annotate the insets with the corresponding physical size at the distance of each galaxy (ranging from 22 – 37 pc on a side). We show the $2''.5$ -diameter COS PSA as a white circle, verifying that all three stars are well-centered and isolated in the aperture, so the extracted COS/FUV spectra will accurately measure photons from the target stars. All target stars are approximately point sources as expected, though some diffuse emission surrounding LP26 is visible in the NUV acquisition image, likely due to the H II region in which the star is embedded.

The three target stars are distant and therefore faint, so multiple visits (up to 5 per grating) were typically required to achieve high enough SNR to detect weak photospheric absorption lines in the continuum. For each star, we resample all spectra onto a common wavelength grid and coadd the spectra across all visits, weighting by the inverse variance. This procedure both increases the SNR and produces a single composite spectrum for each star. The dispersion of the combined spectra is $12.23 \text{ m}\text{\AA}/\text{pixel}$, limited by the dispersion of the G160M grating¹.

We measure the spectral resolution as the FWHM of Gaussian line profiles fit to the Milky Way ISM absorption features in the FUV spectra, specifically Si II 1190, 193, 1260, 1526 Å and C II 1134 Å. Across all three stars we find typical velocity FWHM of $\sim 50 \text{ km s}^{-1}$, corresponding to $R \sim 6000$. This measured FWHM is about three times larger than the theoretical 6-pixel resolution element of $\sim 15 \text{ km s}^{-1}$. Individual absorption components due to the Milky Way and target galaxy ISM can be resolved in the spectra, enabling us to measure the systemic velocity v_{sys} of each host galaxy (reported in Table 2). We choose to bin the coadded spectra by 12 pixels ($\sim 30 \text{ km s}^{-1}$) for all analysis to boost the SNR as much as possible while ensuring 1.5 – 2 samples per resolution element across the entire spectral range. This binning achieves SNR between 6.5 – 10.3, 9.6 – 12.7, and 5.6 – 7.3 at 1170 Å, 1430 Å, and 1560 Å, respectively, with the S3 data reaching the lowest SNR and A15 the highest across the entire FUV wavelength range. Finally, we correct the spectra for Milky Way foreground dust extinction assuming a Fitzpatrick (1999) extinction law with $R_V = 3.1$.

3. ANALYSIS OF FUV SPECTRA AND SPECTRAL ENERGY DISTRIBUTIONS

Here, we present and analyze the new FUV spectra of three low- Z O stars. These include the first such ob-

servations of O dwarfs below $10\% Z_{\odot}$ (LP26 and S3), enabling new constraints the properties of extremely metal-poor, unevolved massive stars. We quantify the strengths of photospheric and wind lines, estimate their projected rotation speeds $v \sin(i)$, and constrain the stars’ fundamental parameters via SED fitting.

3.1. FUV Metal Opacities

Many transitions of metal ions common in hot stellar atmospheres lie in the FUV, including forests of weak Fe lines that dominate the metal opacity. The strengths of these lines are sensitive to the temperature, ionization structure, and metal abundances in the stellar atmospheres. Medium-resolution COS spectroscopy enables detection of even relatively weak lines expected at low Z and empirically constrains the opacity sources in the target stars. Figure 2 presents the co-added and flux-calibrated FUV spectra of the three stars, shown as black lines. Wavelengths have been corrected to the rest frame using the systemic velocity measured for each galaxy from the Gaussian modeling of ISM absorption lines described in Section 2.3 (see Table 6 below). The measurement uncertainties on the spectra are shown as the solid grey lines in each panel. The colored vertical lines indicate the locations of various features in the spectra: photospheric absorption (red), stellar wind absorption and emission (blue), and nebular emission (purple). Grey dashed vertical lines show the locations of ISM absorption at the velocity of the Milky Way. Regions of the spectra contaminated by geocoronal emission lines have been greyed out.

The three FUV spectra are ordered from top to bottom by increasing nebular abundance of the host galaxy. By eye, it is obvious that the continua of the lower- Z LP26 and S3 are quite featureless compared to that of A15, though the most prominent photospheric lines are visible in all three spectra (e.g., C III 1176 Å and He II 1640 Å). The wind-sensitive lines are clearly much more prominent in A15 than in the two lower- Z stars; we discuss this in detail in Section 3.2 below. Nebular emission lines are only present in the spectrum of the lowest- Z star, LP26, as expected since this is the only target star embedded in an H II region.

We quantify the strengths of the photospheric lines by measuring their equivalent widths (EWs), defined as:

$$\text{EW} = \int_{\text{bandpass}} 1 - \left(\frac{F_{\lambda}}{F_{\lambda}^{\text{continuum}}} \right). \quad (1)$$

The feature bandpasses are chosen to cover the entire observed line profile across all three spectra and minimize contamination from nearby ISM and strong photospheric lines predicted by TLUSTY theoretical spectra

¹ <https://hst-docs.stsci.edu/cosihb>

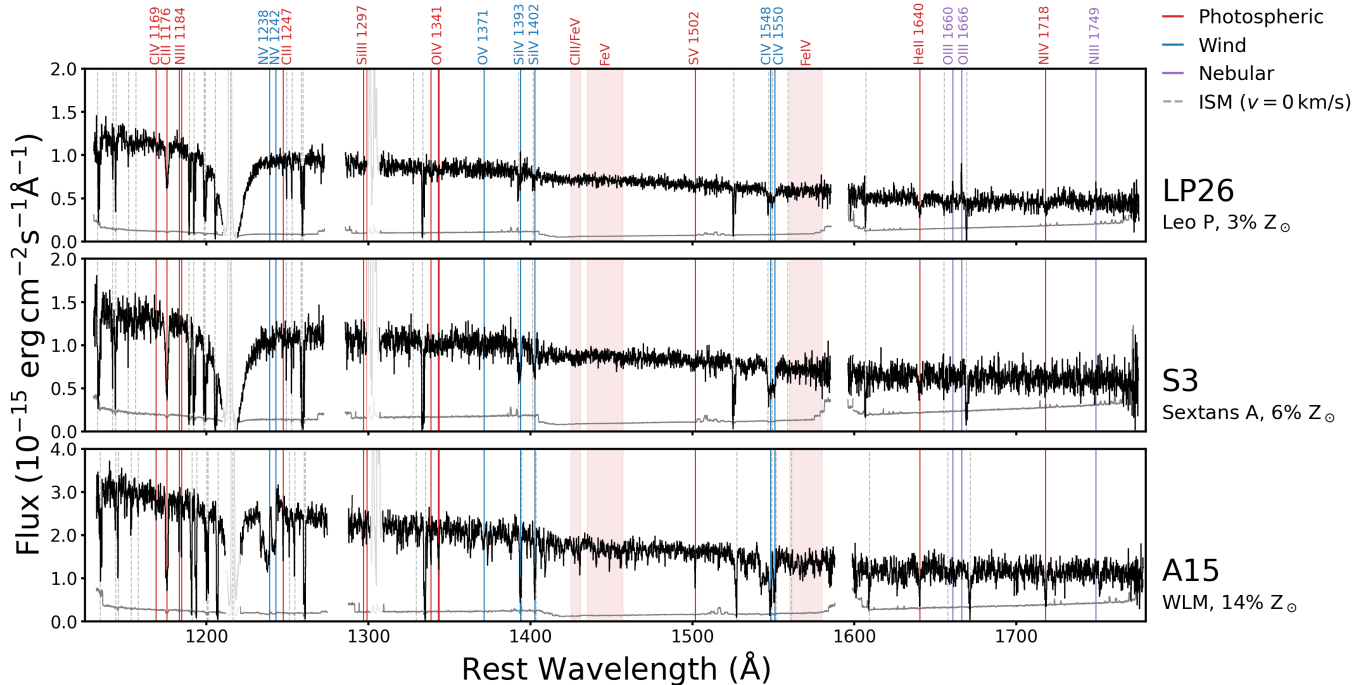


Figure 2. The first FUV spectra of extremely metal-poor O-dwarf stars. The *HST*/COS spectra of our target stars in Leo P (top), Sextans A (middle), and WLM (bottom) are plotted in black as a function of wavelength, corrected to the host galaxy rest frame using the systemic velocity measured from the ISM lines. The uncertainties are shown as the solid grey line in each panel. Spectral regions affected by geocoronal emission lines have been greyed out for clarity, and the locations of Milky Way ISM absorption lines are shown by the grey dashed lines. Stellar photospheric and wind features are indicated by red and blue vertical lines, respectively, and the nebular emission lines visible in the LP26 spectrum are shown by the purple lines. Red shading highlights “forests” of primarily Fe transitions. The increasing line blanketing by Fe-peak elements and increasing wind strength from 3% to 14% Z_{\odot} is evident by eye. The LP26 star is the lowest- Z star ever observed in the FUV, and these data reveal a surprisingly featureless continuum as well as rare nebular emission lines powered by a single O star.

drawn from the OSTAR2002 grid (Lanz & Hubeny 2003). Table 4 reports the rest wavelengths of the adopted feature bandpasses, where the spectra are corrected for the velocity of the stars determined from cross-correlating observed photospheric lines with the transitions in the TLUSTY model spectra (discussed further in Section 3.3 below). The continuum flux level is determined from $1 - 5 \text{ \AA}$ regions on either side of the feature bandpass, similarly chosen to avoid contaminating ISM lines and stellar lines. The continuum bandpasses adopted for all photospheric and wind features are reported in Table A1 in Appendix A. We perform a least-squares linear fit across the continuum bandpasses to estimate the local continuum level around each photospheric line. We resample the flux 1,000 times, adding offsets to the measured flux drawn from a Gaussian distribution with a mean of 0 and a standard deviation equal to the measured flux uncertainty. Continuum levels and EWs are re-measured for all resampled spectra, and the EW uncertainty (σ_{EW}) is defined as the standard deviation of these EW measurements.

Table 4 presents the EW measurements for various photospheric lines in the three stars LP26, S3, and A15. Only EWs measured at the 2σ level are reported; if the SNR is lower, we consider that feature to be undetected and the σ_{EW} is taken to be an upper limit on its EW. Some bandpasses contain multiple transitions of the same ion, indicated with asterisks in Table 4. The last three rows of Table 4 report the EWs of wider “forest” regions that contain a large number of transitions that can eat away at the continuum level: Fe v 1445 \AA , Fe v/C III 1428, and Fe IV 1570 \AA (red shaded regions in Figure 2). Again, we use TLUSTY model spectra to select regions for continuum normalization expected to be free of photospheric line absorption (Table A1). The high density of lines in these forest regions restricts us to narrow ($\lesssim 2 \text{ \AA}$) continuum bandpasses, and these are not guaranteed to sample the true continuum level, though metal line absorption reducing the apparent continuum level should be less problematic at low Z . Interestingly, we only detect the depletion of continuum in these Fe forests for the highest-metallicity star, A15. This is a quantitative confirmation of the visual impression from

Table 4. Equivalent Widths of FUV Photospheric Lines

Feature	LP26		S3		A15		All Stars Feature Bandpass (Å)
	EW (Å)	σ_{EW} (Å)	EW (Å)	σ_{EW} (Å)	EW (Å)	σ_{EW} (Å)	
C III 1176*	0.83	0.09	1.26	0.13	1.04	0.08	1173.5 – 1177.5
N III 1184*	...	0.10	...	0.14	0.24	0.08	1182.5 – 1185.2
C III 1247	0.11	0.05	...	0.07	0.17	0.04	1246.4 – 1248.0
O IV 1341*	0.34	0.17	...	0.23	0.36	0.16	1337.5 – 1344.5
S V 1502	...	0.07	...	0.10	0.21	0.07	1500.5 – 1503.0
He II 1640	0.77	0.30	...	0.34	0.91	0.23	1638.6 – 1643.0
N IV 1718	...	0.28	...	0.34	0.75	0.23	1716.6 – 1719.7
Fe V/C III 1428*	...	0.12	...	0.15	0.73	0.10	1425.0 – 1431.0
Fe V 1445*	...	0.46	...	0.63	1.46	0.41	1435.0 – 1457.0
Fe IV 1570*	...	0.96	...	1.26	1.70	0.54	1560.0 – 1580.0

NOTE—All features included in this table were detected at the 2σ level in at least 1 star. No EW is reported for measurements with lower SNR; in those cases, σ_{EW} is taken to be an upper limit on the EW. Features marked with * contain multiple transitions of the same ion.

Figure 2 that the two very low- Z stars have featureless continua, even in the higher SNR 1400 – 1500 Å range.

Some lines that might be expected in these mid-late O stars (Heap et al. 2006) are not detected in any of the three at the 2σ level, including C IV 1169 Å and the Si III triplet near 1296 Å. This is due to a combination of the weakness of those lines in the low- Z stellar spectra, the SNR of the spectra, and the difficulty of estimating a reliable continuum level for Si III 1296 Å in particular due to its location between a gap in the spectra and prominent O I geocoronal emission. However, the C IV 1169 Å line is in a relatively high SNR region, and upper limits on its EW range from 0.08 to 0.13 Å, with the smallest upper limit found for the highest- Z star, A15. The ratio of C III 1176 Å to C IV 1169 Å is sensitive to T_{eff} (Heap et al. 2006), so this non-detection of C IV 1169 Å may suggest that all three target stars are relatively cool. We return to this point in Section 3.4.2 below.

3.2. Stellar Winds

Resonance lines in the FUV are excellent stellar wind diagnostics, sensitive to both \dot{M}_* and velocity structure. The shapes of the wind profiles give empirical insight into the strength and v_∞ of a stellar wind. P-Cygni wind profiles are produced by wind emission that extends to $\pm v_\infty$ and blueshifted absorption from $-v_\infty$ to zero velocity. v_∞ can therefore be measured empirically from the blueward extent of the “black part” of the absorption trough for fully saturated lines (i.e., absorption that reaches a flux of 0). For unsaturated P-Cygni profiles, the wind may not be optically thick to absorption in the outer, higher velocity regions, and so the blue-

ward extent of the wind absorption represents a lower limit on v_∞ (Lamers et al. 1995; Crowther et al. 2016). The depth of the wind absorption troughs and presence of emission components indicate the density of the wind material, such that stronger wind profiles signal higher \dot{M}_* . Quantitative measurement of \dot{M}_* requires computationally intensive atmosphere modeling that accounts for hydrodynamics, metal abundances, and ionization structure and is beyond the scope of the present work. Here, we discuss the empirical constraints that FUV wind line profiles provide on winds that metal-poor O V stars are capable of driving.

Figure 3 shows the wind-sensitive lines in the COS spectra of the three target stars. Sections of the spectra of LP26 (top/purple), S3 (middle/blue), and A15 (bottom/red) are plotted against velocity relative to the wavelength of the bluest transition in each panel. The spectra have been normalized to a continuum level of 1, then plotted with an integer offset for clarity. We select continuum regions free of photospheric, wind, and ISM lines on either side of each wind-sensitive feature (reported in Table A1 in Appendix A) and perform a linear fit to the local continuum for all lines except N V, which requires a third-order polynomial to capture the shape of the red wing of Lyman α absorption. Vertical dashed lines indicate the relative velocities of each wind line transition, where $v = 0$ is the velocity of the bluest transition in each panel, and diamonds below each spectrum show the velocities of narrow ISM components determined from modeling Si II and C II lines (Section 2.3).

It is clear that A15, which is both the highest- Z and earliest type of the three stars, has the strongest wind

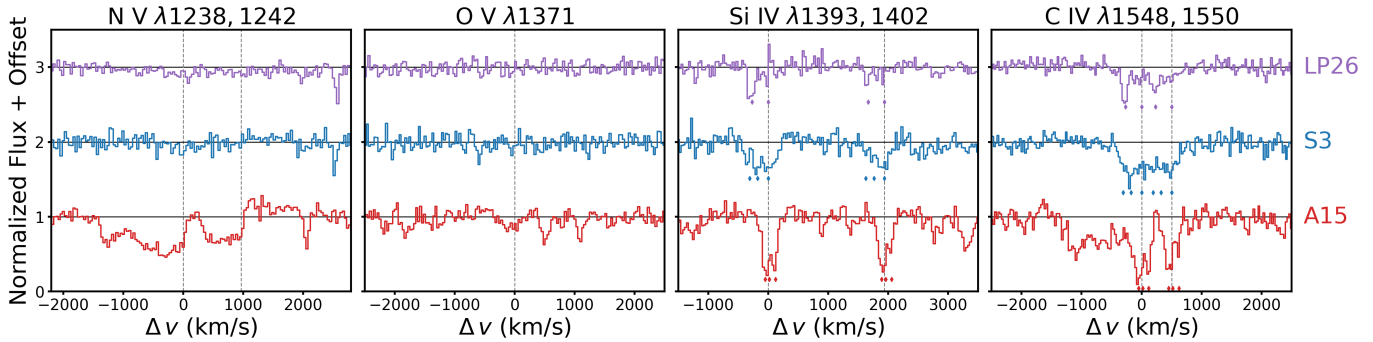


Figure 3. Weak stellar wind features at extremely low metallicity. Continuum-normalized spectra are plotted as a function of velocity offset from the center of wind-sensitive lines, from left to right: N v 1238 Å, O v 1371 Å, Si iv 1393 Å, and C iv 1548 Å. Vertical dashed lines indicate zero velocity for the bluer transition and the velocity of the redder transition in the doublets. The spectra of LP26 (purple), S3 (blue), and A15 (red) are presented in order of increasing Z from top to bottom. Spectra are normalized to a continuum level of 1 (indicated by horizontal black lines), then vertically offset from each other for clarity. Diamonds below each spectrum indicate the velocities of ISM Si II and C II absorption components detected in the spectrum of that star. Broad, blueshifted C IV wind absorption is clearly present in S3 and A15, and possibly also in LP26. A15 also shows wind absorption and emission in the N v and O v lines. All stars’ Si IV lines are likely due to photospheric and ISM absorption rather than winds.

Table 5. FUV Wind Line Properties

Star	Feature	v_{edge} (km s^{-1})	$\sigma_{v_{\text{edge}}}$ (km s^{-1})	EW (Å)	σ_{EW} (Å)	Feature Bandpass (Å)
S3	C IV 1548	440	120
A15	C IV 1548	1370	150
A15	N v 1238	1410	150	2.12	0.10	1233.0 – 1239.8
A15	N v 1242	0.83	0.06	1239.9 – 1243.2
A15	N v 1242 Emission	≤ -0.43	0.07	1243.2 – 1246.7

NOTE—EWs are defined such that absorption is positive and emission is negative. The A15 N v 1242 emission EW is an upper limit because the feature bandpass was truncated to avoid the blended C III 1247 photospheric line.

features. Broad, blueshifted absorption is present in both the N v 1240 Å and C IV 1549 Å lines, as well as redshifted emission in N v. The O v 1371 Å line also appears affected by the stellar wind, with a broad, blueshifted absorption feature bracketed by emission. This weaker, non-resonance transition may only absorb in the denser, lower-velocity part of the wind, leading to blueshifted emission not seen in resonance lines. The EW of O v 1371 Å wind absorption has been used as a T_{eff} diagnostic above ~ 40 kK (de Koter et al. 1998), but the weak absorption strength in the A15 spectrum suggests a cooler T_{eff} than that threshold.

The spectra of the two extremely metal-poor stars reveal weaker wind features. S3 shows broad, blueshifted absorption in the C IV line, but no evidence of wind features in any of the other transitions. LP26, the lowest-metallicity star, shows a hint of broad absorption in C IV, but this feature is weak and its blue edge is contaminated by narrow ISM absorption. Overall, the lowest- Z

star in this sample does not show evidence of strong stellar winds, suggesting very low \dot{M}_* as expected for extremely metal-poor, main-sequence O stars. None of the three spectra show any wind-like features in the Si IV lines, suggesting that their winds are hot and/or low-density (e.g., Chisholm et al. 2019).

We quantify the strength and velocity extent of the clearly detected wind features in Table 5. LP26 is excluded from this analysis due to the very weak (if present at all) wind features in its FUV spectrum and contamination of the C IV feature by strong ISM absorption. We measure v_{edge} for A15 and S3, defined as the velocity where the blue edge of the wind absorption meets the normalized continuum level of 1. This is an approximation of v_{∞} for optically thick winds (e.g., Crowther et al. 2016), or for weaker winds, a measure of the velocity extent of the denser, inner part of the wind. We measure v_{edge} of 450 km s^{-1} from the C IV 1548 Å line in S3’s spectrum, which is much lower than the expected

Table 6. Projected rotation velocities, radial velocities, and host galaxy systemic velocities measured from FUV spectra. Galaxy v_{sys} measurements are repeated from Table 2 to facilitate comparison with stellar v_{radial} .

Star	$v \sin(i)$ (km s^{-1})	v_{radial} (km s^{-1})	Galaxy v_{sys} (km s^{-1})
LP26	370 ± 90	283	248
S3	290 ± 90	296	302
A15	80 ± 45	-145	-115

v_{∞} for an O9 V star, even after accounting for the expected metallicity dependence $v_{\infty} \propto Z^{0.13}$ (Leitherer et al. 1992): scaling the typical v_{∞} for Galactic O9 V stars given by Kudritzki & Puls (2000) gives an expected $v_{\infty} \sim 1040 \text{ km s}^{-1}$ at $6\% Z_{\odot}$. This wind profile is likely under-developed and not optically thick in the outer, fastest regions of the wind, so the empirical v_{edge} measurement underestimates v_{∞} of the wind in S3. A15 has two well-developed wind profiles at N v 1238 Å and C iv 1548 Å. Averaging the measurements for the two lines, we find v_{edge} of 1390 km s^{-1} . The wind lines are not saturated, so this should be treated as an upper limit on v_{∞} . Indeed, our measured v_{edge} is lower than the expected $v_{\infty} \sim 1860 \text{ km s}^{-1}$ for an O7 V star at $14\% Z_{\odot}$, again assuming the Leitherer et al. (1992) scaling. On the other hand, it is consistent with reported v_{∞} measurements as low as 1300 km s^{-1} for O6.5-7 V stars in the SMC (Bouret et al. 2013).

Table 5 also reports the EWs of the N v 1238, 1242 Å absorption and N v 1242 Å emission, which are only detected in the spectrum of A15. These lines are prominent and not contaminated by ISM absorption, though the absorption trough of the redder line is likely impacted by emission due to the bluer line. By convention, the EW of emission is negative, with lower values indicating stronger emission. The N v 1242 Å emission is blended with the C III 1247 Å photospheric line, so we restrict our EW measurement to wavelengths blueward of that line, resulting in an upper limit on the EW (i.e., the emission is at least as strong as the reported EW indicates). Uncertainties on both EW and v_{edge} are estimated from repeating the measurements 1,000 times on spectra resampled from their uncertainty distributions, as explained in Section 3.1.

3.3. Projected Rotation Velocities

The 50 km s^{-1} resolution of the COS spectra enables us to constrain the projected rotation speeds, $v \sin(i)$, of our target stars. Rotation broadens intrinsically narrow absorption lines, changing the shapes of the observed profiles but keeping the EW intact. $v \sin(i)$ can there-

fore be constrained by convolving appropriate theoretical spectra with a rotational broadening kernel to reproduce the observed photospheric line profiles (e.g., Huang & Gies 2006; Bouret et al. 2013). The C III 1176 Å complex is a particularly useful diagnostic, as the six closely spaced lines remain separable at $v \sin(i) \lesssim 40 \text{ km s}^{-1}$ (Heap et al. 2006), and at higher $v \sin(i)$ the shape of the smoothed profile (particularly the wings) remains sensitive to changes in rotation. This line is also the only photospheric feature detected at the 2σ level in all three COS spectra, enabling a uniform measurement technique across the sample. While C III 1176 Å can manifest as a wind line at high Z , previous work on SMC O stars has shown that this transition is free from wind effects at $20\% Z_{\odot}$ (Heap et al. 2006; Bouret et al. 2013), and our *HST*/COS spectra do not show emission or blueshifted absorption in this feature. Thus, we can safely assume that this is a photospheric line suitable for constraining $v \sin(i)$ of our metal-poor target stars.

The unbroadened theoretical spectra we use in this analysis are TLUSTY (Hubeny & Lanz 1995) models drawn from the OSTAR2002 grid² (Lanz & Hubeny 2003). These model atmospheres span a wide range of Z ($0 - 2 Z_{\odot}$, with $Z_{\odot} = 0.017$; Grevesse & Sauval 1998) and include NLTE and line-blanketing effects, but not stellar winds. At each metallicity, theoretical spectra are provided for $27.5 \leq T_{\text{eff}} \leq 55 \text{ kK}$ in steps of 2.5 kK and for $3.0 \leq \log(g) \leq 4.75$ in steps of 0.25 .

For each star, we adopt the OSTAR2002 model with C III 1176 Å EW matched to that measured in its COS spectrum (Table 4). The EW is sensitive to many stellar parameters, including T_{eff} , $\log(g)$, and Z , but the intrinsic profile shape is not sensitive to these properties. We will constrain the stellar parameters from SED fitting in Section 3.4 below, but for now use a simplified selection of appropriate theoretical spectra that reproduce each star’s C III line strength. These $v \sin(i)$ measurements will be used in the SED fitting process to smooth the model spectra; this is necessary to obtain a good match to the FUV continuum level. We have checked that using the OSTAR2002 models corresponding to the best-fit stellar parameters from SED fitting as the base for the $v \sin(i)$ measurements instead of those selected here does not affect our results.

We fix $\log(g)$ to 4.0 for all three stars, as expected for luminosity class V. To approximate the Z of each star based on its host galaxy nebular Z (Table 1), we adopt the S, V, and W ($1/5$, $1/30$, and $1/50 Z_{\odot}$) grids for A15, S3, and LP26, respectively. These are also the

² <http://tlusty.oca.eu/Thusty2002/tlusty-frames-OS02.html>

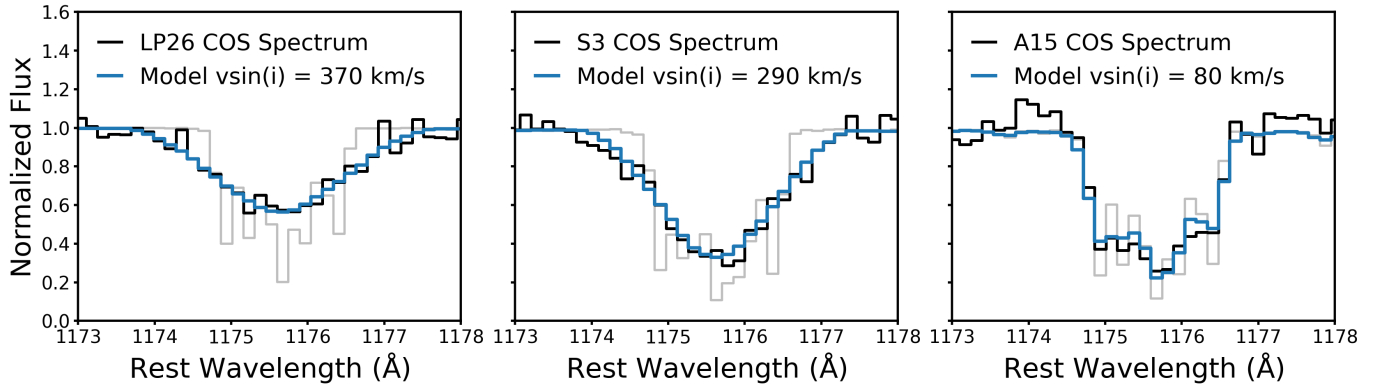


Figure 4. Both extremely metal-poor stars are fast rotators. The continuum-normalized COS spectra around the complex of photospheric C III around 1176 Å are shown as black lines for LP26, S3, and A15 (left to right). The grey line in each panel shows the TLUSTY model that most closely matches the measured C III 1176 Å equivalent width for each star with no rotation, broadened to COS resolution and resampled to the same wavelength grid as the data. The blue line in each panel shows the rotationally broadened TLUSTY model that best reproduces the observed C III profile, and the best-fit $v \sin(i)$ for each star is reported in the legends. High $v \sin(i)$ is required to match the smooth and broad profiles in the LP26 and S3 spectra.

Z grids that we find best reproduce the stellar SEDs in Section 3.4 below. Finally, we search over all available T_{eff} and select the model with the C III 1176 Å EW that most closely matches the measured EW. This selection process resulted in using theoretical spectra with T_{eff} of 40, 35, and 37.5 kK as the base models for A15, S3, and LP26, respectively. These are within the uncertainties of the best-fit T_{eff} from SED modeling, discussed below.

We use the IDL routine `lsf_rotate.pro`³ (reimplemented in Python) to generate rotational broadening profiles. A linear limb-darkening law is assumed (equation 17.11 in Gray 1992) with limb-darkening coefficient $\epsilon = 0.6$ constant across the disk. We convolve the rotationally broadened model spectra with a Gaussian of 50 km s^{-1} FWHM to account for the COS instrumental resolution. We use a least-squares routine to fit for the $v \sin(i)$ and stellar radial velocity (v_{radial}) that produce the best match between the broadened TLUSTY model spectra and the observed C III 1176 Å profiles for the three target stars. The best-fit $v \sin(i)$ and v_{radial} are reported in Table 6. We also repeat the host galaxy systemic velocities (v_{sys} ; initially reported in Table 2 above) determined from fitting the ISM lines (Section 2.3) for comparison to the measured stellar v_{radial} and find only small velocity offsets between our target stars and their host galaxies, $\leq 35 \text{ km s}^{-1}$.

Figure 4 shows the best-fit broadened TLUSTY C III 1176 Å profiles for the three stars. The observed spectra are shown in black and the best-fit models in blue, with the inferred $v \sin(i)$ reported in the legends in each panel, rounded to the nearest 10 km s^{-1} . The

light grey shows the TLUSTY models with $v \sin(i) = 0$, broadened to COS resolution. The highly structured C III 1176 Å profile in A15 indicates a lower $v \sin(i)$ than in S3 and LP26, both of which have smoother profiles with broad wings. The high $v \sin(i) \geq 290 \text{ km s}^{-1}$ for the both of the lower-Z targets is somewhat surprising relative to the observed typical $v \sin(i) \lesssim 120 \text{ km s}^{-1}$ in the Milky Way and Magellanic Clouds, though comparable and even higher $v \sin(i)$ have been measured for OB stars in all three galaxies (e.g., Penny & Gies 2009; Ramírez-Agudelo et al. 2013; Ramachandran et al. 2019). We discuss implications of this finding in Section 4.3.2 below.

The uncertainty in $v \sin(i)$ is dominated by modeling choices rather than measurement uncertainties. We estimate uncertainties by repeating the $v \sin(i)$ and v_{radial} measurements using different TLUSTY base models, changing T_{eff} by one step in the grid ($\pm 2500 \text{ K}$), which changes the C III 1176 Å by about 0.2 Å (larger than the uncertainties on our EW measurements; see Table 4). This exercise results in changes of $\pm 90 \text{ km s}^{-1}$ in $v \sin(i)$ for both of the fast-rotating stars LP26 and S3, so we adopt this value as a conservative estimate of the uncertainty in those measurements. For the lower- $v \sin(i)$ A15, however, the change due to model choice is only $\pm 10 \text{ km s}^{-1}$. The uncertainty in $v \sin(i)$ for A15 is likely dominated by the possible contribution of other broadening mechanisms, which we discuss in the next paragraph. We also check the impact of several modifications to the fitting method: first, including the He II 1640 Å line in the modeling (the only other photospheric feature whose profile is discernible by eye in all three spectra); second, allowing the continuum level to be a free parameter in the modeling; and third, using

³ https://idlastro.gsfc.nasa.gov/ftp/pro/astro/lsf_rotate.pro

the TLUSTY models with T_{eff} and $\log(g)$ determined from our SED fitting in Section 3.4 below. All of these result in differences no larger than $\pm 20 \text{ km s}^{-1}$ in $v \sin(i)$. The v_{radial} is consistent within a few km s^{-1} across all of these tests and is thus insensitive to model choice.

A caveat is that rotation is not the only mechanism that broadens spectral lines: macroturbulence and microturbulence also contribute. The OSTAR2002 model grid was computed with a fixed microturbulent velocity of 10 km s^{-1} , a fairly typical value for mid-late O dwarfs; this process is not expected to dominate the observed line profiles. The relative contributions of rotation and macroturbulence can be separated by measuring $v \sin(i)$ using the Fourier transform method (Gray 1976). Unfortunately, the SNR and spectral resolution of our COS data are not sufficient to enable this more precise measurement of $v \sin(i)$. Simón-Díaz & Herrero (2014) suggest that derived $v \sin(i)$ for O stars that do not account for macroturbulent broadening should be revised downward by $5\text{--}45 \text{ km s}^{-1}$ for $v \sin(i)$ below 120 km s^{-1} . Though the mechanism behind macroturbulence is not settled, there are observational hints that macroturbulence contributes less to broadening with decreasing metallicity and in less evolved stars (e.g., Penny & Gies 2009). Furthermore, Bouret et al. (2013) found agreement within the error bars between $v \sin(i)$ measured for SMC O dwarfs using the Fourier transform technique and by fitting rotationally broadened models, similar to our analysis here. Our measured $v \sin(i)$ should therefore be taken as upper limits, and the true $v \sin(i)$ of A15 may be significantly lower than inferred from our modeling. We therefore adopt $\pm 45 \text{ km s}^{-1}$ as a conservative estimate of the uncertainty on our $v \sin(i)$ measurement for A15. But importantly, the contribution of macroturbulence would not strongly affect the higher $v \sin(i)$ measurements, so our conclusion that S3 and LP26 are fast rotators remains secure.

3.4. Estimates of Stellar Parameters from SED Fitting

To connect the observed FUV spectral features to the physical properties of the stars, we next model their SEDs. This technique is widely used to constrain the luminosity (L_{\star}) of a star in particular, and can also estimate its T_{eff} , $\log(g)$, initial mass (M_{\star}), and age. We simultaneously fit the continuum of the FUV spectra and the NUV, optical, and NIR photometry measured from *HST* imaging of the three stars. All ISM, nebular emission, and wind-sensitive features are masked in the COS spectra, and the observations are corrected for Milky Way foreground extinction (Section 2). In this section, we describe our SED modeling procedure, then present the stellar properties inferred from the best-fit

models and check the fit quality by comparing model-predicted and observed FUV photospheric line profiles.

3.4.1. Description of the Modeling

We construct model SEDs using the TLUSTY OSTAR2002 atmosphere model grid (described in Section 3.3 above), which provides theoretical stellar SEDs and detailed spectra as a function of T_{eff} , $\log(g)$, and Z . The stellar Z dictates the strength of photospheric metal lines as well as the T_{eff} and structure of a star, such that a lower- Z star at fixed M_{\star} and age will be hotter and more compact. Assuming a solar oxygen-to-metals ratio, the nebular abundances of the host galaxies (Table 1) each fall between two of the available Z values in the OSTAR2002 grid, which adopts $Z_{\odot} = 0.017$ (Grevesse & Sauval 1998). We therefore test models at the two Z values bracketing the nebular abundances for each star: the S and T grids ($1/5$ and $1/10 Z_{\odot}$) for A15; the T and V ($1/30 Z_{\odot}$) grids for S3, and the V and W ($1/50 Z_{\odot}$) grids for LP26.

In addition to the parameters of the star itself, dust extinction internal to the host galaxy also affects the overall shape of the stellar SED and must be accounted for in the modeling. Dust extinction laws are known to vary widely, even among various lines of sight within the Milky Way (e.g., Cardelli et al. 1989). It is therefore common to simply adopt a standard Milky Way extinction law, even when modeling stars in external galaxies, given the large uncertainty in the true shape of the extinction law. However, the lower- Z environments of the Magellanic Clouds are known to have different extinction laws, and these may be more appropriate to use when modeling stars in external, metal-poor galaxies. We test both a Fitzpatrick (1999) Milky Way extinction law ($F99$; $R_V = 3.1$) and a steeper Gordon et al. (2003) SMC bar extinction law ($G03$; $R_V = 2.74$) for each star.

We repeat the SED fitting procedure described below for the four combinations of Z and extinction law, and visually inspect each fit to select that which results in the best match to the continuum shape and photospheric line profiles in the FUV spectra. The final adopted Z and extinction law for each star are reported in Table 7.

The TLUSTY SED corresponding to each T_{eff} and $\log(g)$ pair is broadened to the measured $v \sin(i)$ and 50 km s^{-1} COS resolution and shifted to the v_{radial} of each star (Table 6). The models provide the Eddington flux H_{ν} at the stellar surface ($\text{erg s}^{-1} \text{ cm}^{-2} \text{ Hz}^{-1}$), which must be scaled by $(R_{\star}/D)^2$, where R_{\star} is the stellar radius and D is the distance to the star, to obtain the flux that would be measured by an observer. We fix D to the host galaxy distance obtained from the measured magnitude of the tip of the red-giant branch (TRGB; Ta-

Table 7. Best-Fit Stellar Parameters from SED Modeling

Star	OSTAR2002 Grid, Z/Z_{\odot}	Extinction Law	T_{eff} (kK)	$\log(g)$ (cm s^{-2})	A_V^{host} (mag)	$f_{\text{FUV}}^{\text{nebular}}$	R_{\star} (R_{\odot})	M_{\star}^{init} (M_{\odot})	Age (Myr)	$\log(L_{\star})$ (L_{\odot})
LP26	W, 2%	F99	$37.5_{-5.5}^{+5.9}$	$4.00_{-0.24}^{+0.17}$	$0.01_{-0.01}^{+0.06}$	$0.19_{-0.01}^{+0.06}$	$8.2_{-0.4}^{+1.3}$	22_{-5}^{+7}	7_{-3}^{+4}	$5.1_{-0.2}^{+0.2}$
S3	V, 3%	F99	$32.5_{-3.0}^{+2.9}$	$3.50_{-0.15}^{+0.08}$	$0.15_{-0.04}^{+0.08}$	$0.03_{-0.02}^{+0.05}$	$12.1_{-0.3}^{+1.5}$	21_{-2}^{+4}	9_{-2}^{+1}	$5.1_{-0.1}^{+0.2}$
A15	S, 20%	G03	$37.5_{-2.7}^{+7.2}$	$4.00_{-0.10}^{+0.22}$	$0.05_{-0.01}^{+0.06}$	$0.00_{-0.00}^{+0.16}$	$9.5_{-0.9}^{+0.5}$	29_{-3}^{+13}	4_{-3}^{+1}	$5.3_{-0.1}^{+0.2}$

NOTE—The OSTAR2002 grid Z (reported relative to $Z_{\odot} = 0.0017$; Grevesse & Sauval 1998) and extinction law are chosen for each star to best reproduce the observed FUV spectral features. We adopt the Fitzpatrick (1999) law with $R_V = 3.1$ (F99) for LP26 and S3 and the Gordon et al. (2003) law with $R_V = 2.74$ (G03) for A15. The center five columns give the best-fit parameters from our SED modeling, while the last three columns report parameters of the PARSEC model with R_{\star} that gives the best SED normalization.

ble 1). The expected range in R_{\star} near each $T_{\text{eff}}/\log(g)$ grid point is obtained from the PARSEC stellar evolution models⁴ (Bressan et al. 2012). We use isochrones spaced 0.05 dex in $\log(\text{age})$ and densely sampled in M_{\star} interpolated to the metallicities of the OSTAR2002 models. Each sample from these evolution models has an associated R_{\star} , M_{\star} , L_{\star} , and age. The R_{\star} of all PARSEC models falling within half a grid step of each T_{eff} and $\log(g)$ pair (± 1.25 kK and ± 0.125 dex, respectively) are used to scale the TLUSTY SED at that grid point to generate a set of model SEDs with a realistic range of possible flux normalizations.

The final ingredient in the SED models is the contribution of nebular continuum emission in the FUV. Any nebular emission within the 2'5 COS aperture will contribute to the observed FUV spectrum, but the nebular contribution is removed from the NUV-NIR photometry by DOLPHOT's local background subtraction. This is important for LP26 in particular, as this star powers a bright H II region; its NUV acquisition image inset in Figure 1 shows some extended emission within the COS aperture. We use FSPS, an SPS code that self-consistently models stellar populations and the nebular emission they power (Conroy et al. 2009; Byler et al. 2017), to calculate the fractional contribution of the nebular continuum to the total (stellar + nebular) flux in the FUV. Over a range of stellar population Z , maximum M_{\star} , and age, we find that a simple polynomial model describes the shape of the fractional contribution of the nebular continuum as a function of wavelength, with normalization (i.e., the maximum fractional contribution in the FUV) $f_{\text{FUV}}^{\text{nebular}}$. The nebular contribution is larger at redder FUV wavelengths and is negligible blueward of 1216 Å. To account for the nebular contin-

uum in the SED fitting, between $1216 \leq \lambda \leq 1800$ Å only, the model spectrum is multiplied by

$$1 + f_{\text{FUV}}^{\text{nebular}} (-6.012 + 0.008\lambda - 2.231 \times 10^{-6}\lambda^2). \quad (2)$$

For every R_{\star} , T_{eff} , and $\log(g)$ combination, we use a least-squares algorithm to optimize two free parameters: the amount of dust extinction in the host galaxy, parameterized by A_V , and $f_{\text{FUV}}^{\text{nebular}}$. We use photometry tools implemented in the BEAST (Gordon et al. 2016), a Bayesian stellar SED fitting code optimized for *HST* photometry (but not spectroscopy), to measure the flux of the scaled TLUSTY SEDs integrated over the *HST* filters in which we have observed photometry. Finally, we compute the χ^2 goodness-of-fit metric,

$$\chi^2 = \sum_i^N \left(\frac{\text{obs}_i - \text{model}_i}{\sigma_{\text{obs},i}} \right)^2, \quad (3)$$

where N is the number of data points, for each $T_{\text{eff}}/\log(g)/R_{\star}$ combination with optimized A_V and $f_{\text{FUV}}^{\text{nebular}}$. The uncertainties on the photometry are much smaller than on the spectroscopy, so using the χ^2 metric weights the photometry more to balance the smaller number of photometric samples (4 or 5, vs. ~ 3000 in the COS spectra). The model with the lowest χ^2 is adopted as the best fit to the data.

3.4.2. SED Fitting Results

The SED fitting procedure is performed four times for each star, with two different extinction laws and stellar Z (as described in Section 3.4.1 above). We visually inspect the fits to select the extinction law and Z that provide the best match to the normalization and photospheric line profiles in the observed FUV spectra. The parameters of the model that minimized χ^2 for each star for the adopted extinction law and Z are reported in Table 7. Figure 5 presents the SED fitting results for LP26 (top), S3 (middle), and A15 (bottom). The top

⁴ http://stev.oapd.inaf.it/cgi-bin/cmd_3.1

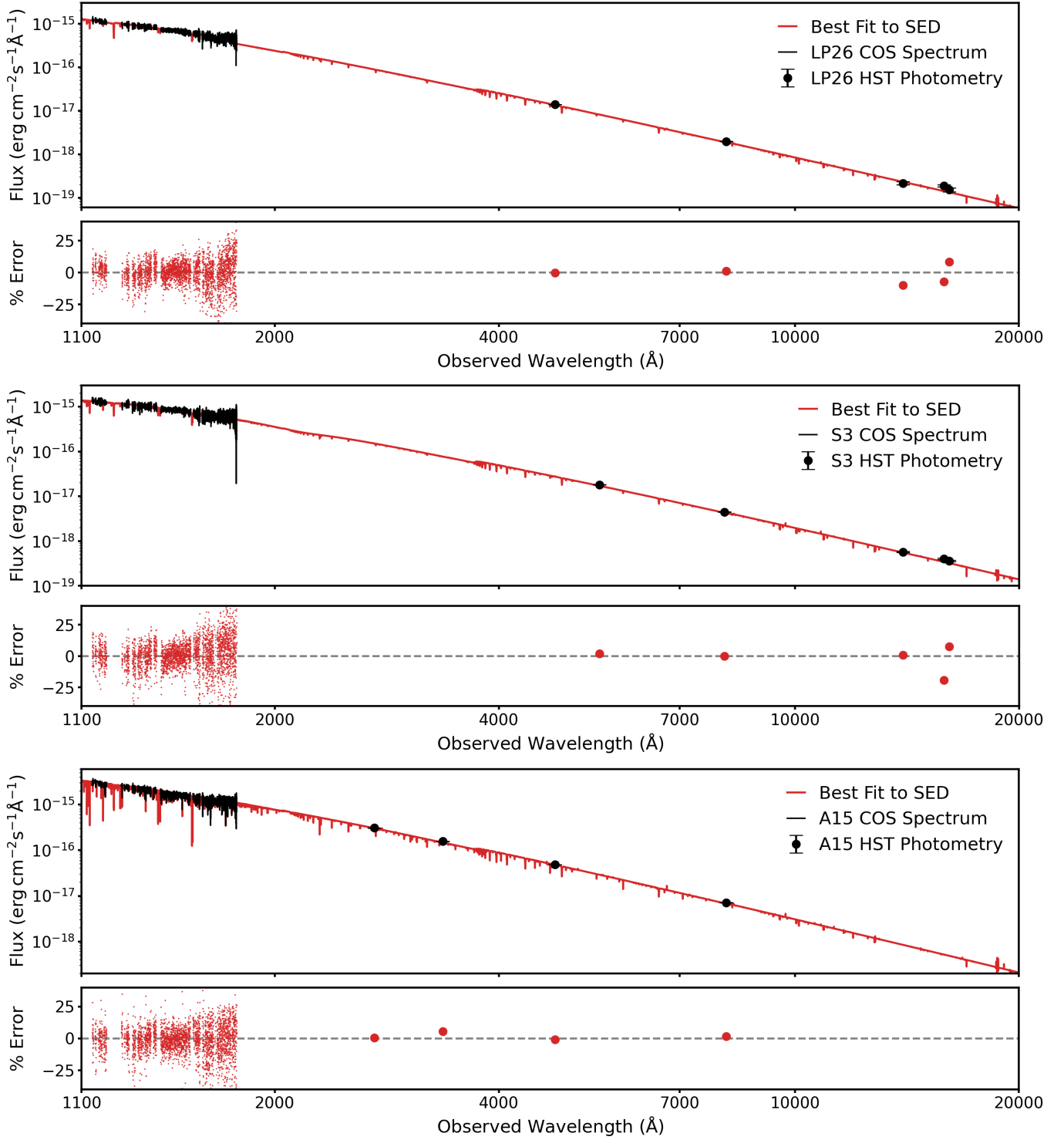


Figure 5. Models fit to the observed stellar SEDs. From top to bottom, each pair of panels shows SED fitting results for LP26, S3, and A15. The observed FUV spectrum and *HST* photometry (black line and points with error bars, respectively) and best-fit SED model (red line) are shown in the top panel of each pair, and the percent errors are plotted as a function of wavelength in the bottom panel, with a dashed grey line at zero error for reference. The fit quality is quite good with errors well-distributed about zero over the full wavelength range. Parameters of the best-fit models are reported in Table 7.

panel in each pair compares the best-fit SED model (red line) to the data (black line and points) as a function

of observed wavelength. Error bars on the photometry are smaller than the point size, though noticeably larger

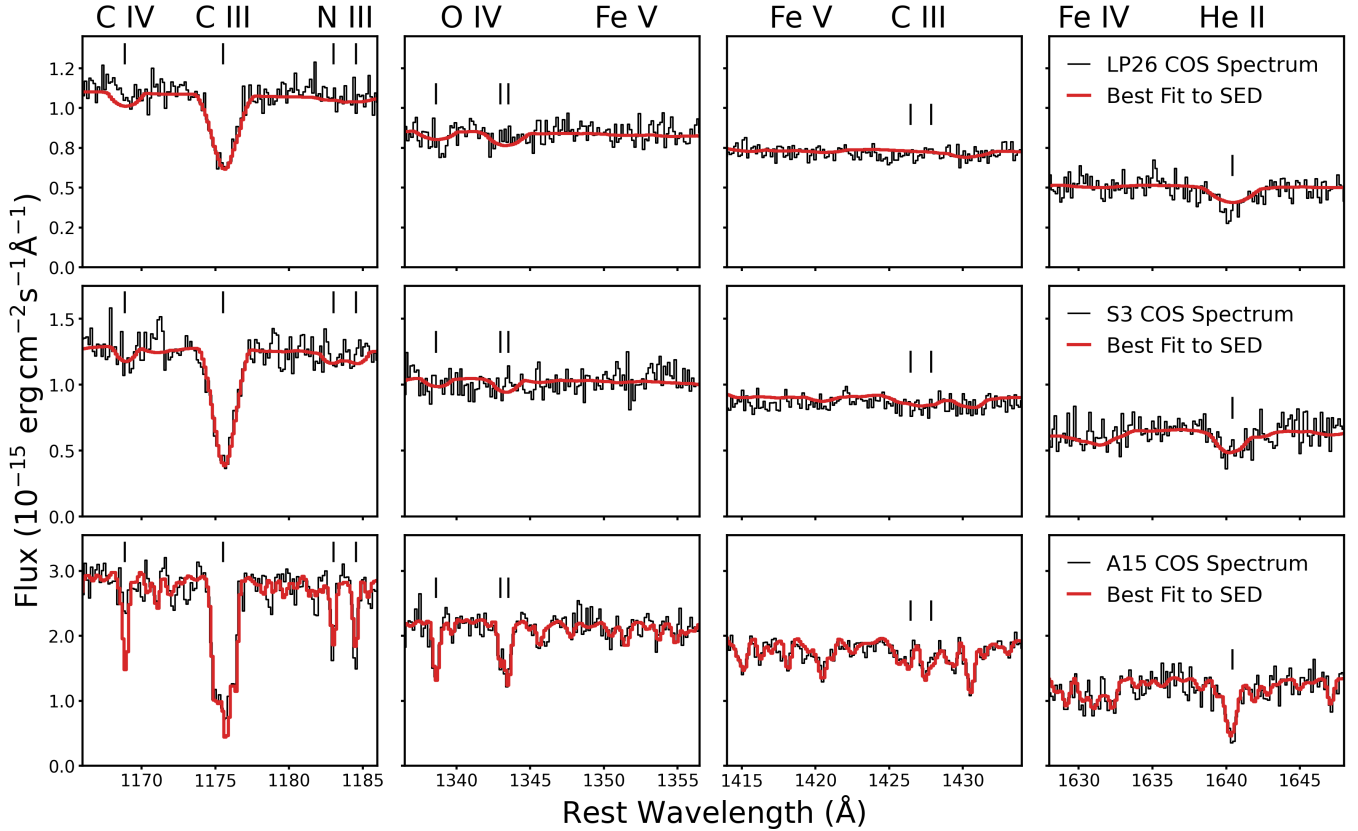


Figure 6. Comparing the best-fit SED models to observed FUV photospheric features. From top to bottom, the observed COS spectra of LP26, S3, and A15 are shown as black lines and the best-fit models from SED fitting, convolved with the $v \sin(i)$ measured for each star (Table 6) and instrumental resolution, are overlaid in red. From left to right, each panel shows a small region of the spectrum focused on photospheric lines that can be used to assess consistency between the SED-based stellar parameters and the FUV properties of the stars. The wavelengths of strong photospheric lines are indicated with black vertical lines in each panel, while Fe forest regions which are simply labeled at the top of the plot. Overall, the agreement is excellent given that the model spectra are drawn from the OSTAR2002 grid and the atmosphere model parameters were not tuned to match the spectral lines.

in the NIR than in the optical and NUV. The bottom panel shows the percent error (red points), where a positive value indicates that the model under-predicts the observation. A horizontal line at zero error, or a perfect match to the data, is shown in the bottom panels for reference. Figure 5 demonstrates that we were able to achieve good fits to the observations for all three targets. The FUV and longer-wavelength fluxes are simultaneously matched and the residuals are centered about zero and not obviously structured. The larger spread in percent error in the FUV is indicative of the lower SNR of the COS data relative to that of the photometry.

Figure 6 presents a detailed comparison between the best-fit models and photospheric features in the FUV spectra. The observed spectra (black) and the best-fit models (red) are plotted as a function of rest wavelength for LP26, S3, and A15, increasing in Z from top to bottom. Model spectra have been broadened to the measured $v \sin(i)$ and COS resolution. Each panel from left

to right shows a small portion of the FUV spectrum centered on photospheric transitions sensitive to stellar properties like T_{eff} , $\log(g)$, and metal abundances.

Figure 6 demonstrates remarkably good agreement with the photospheric line profiles in the observed COS spectra, particularly given that the model spectra were constructed from a pre-computed model grid and that no stellar atmosphere parameters (e.g., individual metal abundances, microturbulence) were tuned to match the observations. The continuum levels are matched well, which suggests that our choice of distances, extinction laws, and parameterization of the FUV nebular continuum are sound. The most notable discrepancy is in the C IV 1169 Å line in A15 (bottom left panel), which is predicted to be much stronger than observed; the cause of this mismatch is not obvious, but future detailed atmosphere modeling of this star should provide insight. Overall, this comparison demonstrates that the OSTAR2002 grid can successfully reproduce the observed

photospheric features of O-dwarf stars at very low Z and supports the validity of our stellar parameter inference. The ability of the OSTAR2002 model spectra to match the FUV line profiles at such low Z is an important victory, given their widespread use in SPS codes that are used to interpret metal-poor stellar populations (e.g., Gutkin et al. 2016) and in galaxy formation models (e.g., Emerick et al. 2019).

The stellar parameters inferred from the best-fit models are fairly similar across the sample: all three stars have relatively low M_* ($\lesssim 30 M_\odot$) and T_{eff} ($\lesssim 40$ kK), consistent with their mid-late O spectral types. LP26 and A15 both appear to be midway through their main-sequence lifetimes, while the modeling suggests that S3 is more evolved and may be leaving the main sequence. None of the stars appears to be particularly young, with best-fit ages ranging from 4 to 9 Myr, which is not surprising, as these stars do not inhabit vigorously star-forming regions. The models prefer very low internal dust extinction in the host galaxies, consistent with expectations for low- Z dwarf irregulars. Only the fit to LP26 requires a large contribution of the nebular continuum in the FUV; the other two stars are fit well with $f_{\text{FUV}}^{\text{nebular}}$ fixed to zero. This is sensible, since LP26 is powering a bright H II region while the other two stars appear far from bright emission in H α imaging.

To estimate the uncertainty on our inferred parameters, we use the range in parameters of all models that agreed with the best-fit model within $\sim 10\%$ for *both* the photometry and spectroscopy. Specifically, we required that neither χ^2_{phot} nor χ^2_{spec} increased by more than $1.2N$ of the minimum χ^2 , where the number of samples N is four or five for the photometry and typically ~ 3000 for the COS spectra. We adopt the difference between 16th and 84th percentile values of the distribution for each parameter and the best-fit value as the uncertainties on the measurement, reported in Table 7. While the uncertainties on the SED-based T_{eff} are rather large ($\pm 3 - 7$ kK), the inferred T_{eff} for the three stars agree within the scatter with scalings between T_{eff} and spectral type at low Z in the literature (e.g., Doran et al. 2013; Ramachandran et al. 2019).

Finally, we acknowledge that neither rotation nor binary effects were accounted for in the SED analysis. The PARSEC stellar evolution models do not include rotation, but their flexibility in Z , M_* , and age sampling relative to other available evolution models was essential for the modeling technique used in this work. Rotation should only mildly affect the stellar properties associated with a star’s position on the Hertzsprung-Russell diagram during its main sequence lifetime (e.g., Brott et al. 2011; Groh et al. 2019), potentially causing an underestimate

of stellar age by up to 1 Myr and an overestimate of M_* by a few M_\odot (Camacho et al. 2016). This level of systematic uncertainty is within our conservatively estimated error budget. It is also possible that any (or all) of our sample stars could have undetected binary companions, but the available data do not suggest that we need to account for a companion in the SED fitting.

4. DISCUSSION

4.1. Comparison to Analog Stars in the SMC

Comparing our new FUV spectra of O V stars in 3 – 14% Z_\odot galaxies to FUV observations of similar stars in the 20% Z_\odot SMC provides an empirical demonstration of the impact of Z on photospheric and wind features. The known spectral types of the target stars and measurements of their stellar properties presented in Section 3.4.2 enable us to identify similar stars in the SMC. For each low- Z target, we selected two analog stars from the sample of O dwarfs in the SMC analyzed by Bouret et al. (2013), for which *HST*/COS observations are available (GO-11625; PI: I. Hubeny). The SMC stars’ fundamental properties, abundances, winds, and rotation were characterized with CMFGEN (Hillier & Miller 1998) atmosphere models fit to their FUV (and optical, where available) spectra. All stars in the Bouret et al. (2013) sample have $\log(g)$ close to 4.0, but span a wide range in other properties. We matched the SMC stars to our targets as closely as possible in spectral type, T_{eff} , and $v \sin(i)$ to control for properties other than Z that affect the morphology of spectral lines.

Figure 7 compares the FUV spectra of each of our target stars to its two analogs in the SMC. In each row, the black line shows the spectrum of one of our targets (LP26, S3, and A15, increasing in Z from top to bottom) and the *HST*/COS spectra of two comparison stars drawn from the Bouret et al. (2013) sample are shown as red and blue lines. Each column shows a small wavelength range containing transitions sensitive to the star’s photospheric conditions and/or wind strength. The strong wind and photospheric lines are indicated at the top of each panel with vertical black lines (except for the many Fe IV transitions in the right column) and labeled at the top of the figure. All spectra have been shifted to the star’s rest wavelength and have been normalized to a continuum level of 1. The spectra have been offset by integer values for clarity and the horizontal lines show the continuum level of each spectrum for reference. Labels at the right side of the figure give the name of each star and its properties that we used to construct this comparison.

We can now use these matched samples to assess the impact of metallicity on the FUV spectral morphology

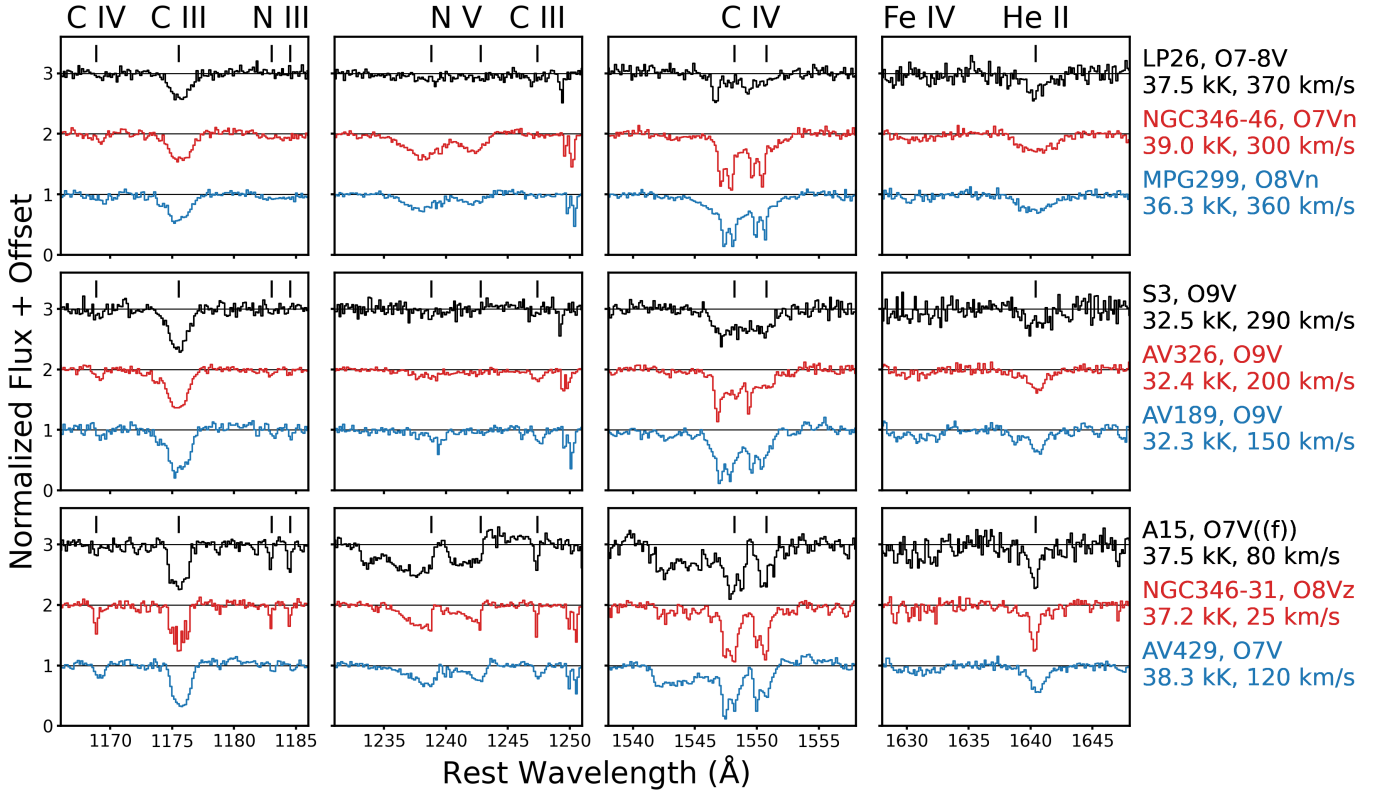


Figure 7. Comparing the FUV spectra of low- Z O dwarfs to SMC analogs. Each row shows the continuum-normalized COS spectrum of one of our target stars in black (from top to bottom: LP26, S3, and A15) alongside the normalized spectra of two O dwarfs in the 20% Z_{\odot} SMC in red and blue, offset for clarity. The comparison stars were matched as closely as possible in spectral type, T_{eff} , and $v \sin(i)$ to the inferred parameters for our target stars (values are reported in the labels to the right of each row). Each panel shows a small region of the FUV spectrum containing photospheric and/or wind-sensitive lines, which are indicated with black vertical lines in each panel. The spectra of S3 and A15 appear surprisingly similar to their SMC analogs, but the wind lines in LP26 are far weaker than SMC stars with similar photospheric line strengths.

for otherwise similar O V stars. Beginning with LP26 (3% Z_{\odot}) in the top row, the photospheric features in the left and right panels appear similar across the three stars, including the smooth and broad profiles due to high $v \sin(i)$ (Section 3.3). This comparison to fast rotators in the SMC emphasizes the fact that high $v \sin(i)$ can broaden weak photospheric lines to the extent that they become undetectable above the noise level in the continuum, at least partly accounting for the observed featureless continuum in LP26. The wind-sensitive features in the center two panels, however, reveal a strong difference in wind strength between LP26 and the two higher-metallicity SMC stars. This is qualitatively consistent with expectations from line-driven wind theory.

Turning to S3 (6% Z_{\odot}) in the middle row, both the wind and photospheric features appear similar across the three stars. The measured $v \sin(i)$ for S3 is higher than that of any O9 V stars in the Bouret et al. (2013) sample, accounting for the somewhat broader C III 1176 Å and He II 1640 Å lines. The wind-sensitive features also show little difference across the three stars, in the sense that

they are all very weak. None of the spectra shows broad wind absorption in N V 1240 Å, and all three C IV 1550 Å wind profiles have a small velocity extent, suggesting that the winds become optically thin in the lower-density outer regions. The narrow C IV 1550 Å absorption components due to the ISM of the host galaxies and the Milky Way appear stronger in the spectra of the SMC stars, but the broad wind absorption profiles are similar for S3 and its two SMC analogs. These are the latest spectral types in our analysis, so the finding of winds with similarly low optical depths across more than a factor of two difference in Z is not surprising.

Finally, the comparison for A15 (14% Z_{\odot}) in the bottom row tells a rather different story: both of its strong wind lines actually appear stronger than those of the SMC stars (center two panels). The absorption is deeper and extends blueward to higher velocities, suggesting a higher \dot{M}_{\star} than in its SMC counterparts. Some of the photospheric metal lines appear stronger as well (specifically N III 1183, 1184 Å in the left panel and the Fe IV lines in the right panel), though notably the C IV 1169 Å

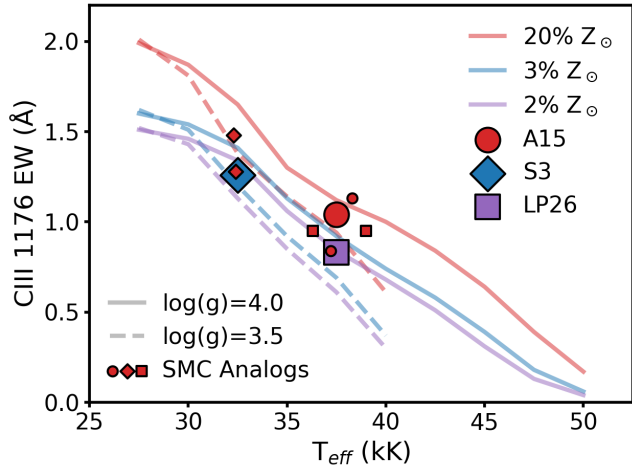


Figure 8. C III 1176 Å EW in the target stars compared to their SMC analogs. C III 1176 Å EW plotted as a function of T_{eff} for stars in our low- Z sample (large points) and their SMC analogs (small points, marker shape matched to that of their associated low- Z star). Lines show C III 1176 Å EW measured from theoretical TLUSTY spectra, where solid and dashed lines indicate $\log(g)$ of 4.0 and 3.5, respectively. Color-coding indicates Z of the TLUSTY models, with red, blue, and purple corresponding to 20%, 3%, and 2% Z_{\odot} , respectively. Markers for the observed stars are colored according to the Z adopted in the SED fitting, or assuming 20% Z_{\odot} for the SMC analogs. The C III 1176 Å EWs for LP26 and S3 are smaller than those measured in their SMC analogs, while A15’s EW is intermediate between those of its SMC counterparts. Overall, C III 1176 Å EW is more sensitive to T_{eff} than Z or $\log(g)$, suggesting this can be a useful diagnostic of stellar population T_{eff} and age in FUV observations of metal-poor galaxies.

line is much weaker in A15 than in the SMC analogs. The best-fit TLUSTY SED model also failed to reproduce that weak line (Section 3.4.2), making A15 an intriguing object for further study with detailed atmosphere models. Overall, this comparison strongly suggests that A15 is at least as metal-rich as the SMC analog stars; we discuss this finding in the context of previous work on O stars in WLM in Section 4.2 below. The two SMC analogs bracket A15 in $v \sin(i)$, and the fact that the structure of A15’s C III 1176 Å feature is intermediate between that of the two comparison stars supports our measured $v \sin(i)$.

It is interesting that the strong photospheric lines in all three low- Z target stars appear similar to those of their comparison stars in the SMC. As the C III 1176 Å line is the only one formally detected in all three of our *HST*/COS spectra, we focus our quantitative comparison on this feature. Figure 8 shows the measured C III 1176 Å EWs for our metal-poor O dwarfs (large markers, where the red circle, blue diamond, and purple

square indicate A15, S3, and LP26, respectively) and for their SMC analog stars (small red markers, with shapes matched to those of the target stars against which they are compared) as a function of T_{eff} . For comparison, the lines show C III 1176 Å EWs measured from TLUSTY spectra drawn from the OSTAR2002 grid as a function of the model T_{eff} , with solid and dashed lines indicating $\log(g)$ of 4.0 and 3.5, respectively. The lines are color-coded by the metallicity of the TLUSTY models, with red, blue, and purple corresponding to 20%, 3%, and 2% Z_{\odot} , respectively. Markers for the target stars are colored to match the Z of the TLUSTY model adopted in fitting their SEDs, and SMC stars are all colored red to indicate their 20% Z_{\odot} .

First, the measured C III 1176 Å EWs agree well with the EWs predicted by their best-fit TLUSTY models, confirming the qualitative agreement in Figure 6. Next, we compare the C III 1176 Å EW of each metal-poor target star to those of its SMC analogs. Both LP26 and S3 have EWs smaller than those of their higher- Z SMC counterparts at similar T_{eff} , consistent with the metal-poor stars having lower C abundances. The C III 1176 Å EW of A15, on the other hand, is between those of its two comparison stars in the SMC, suggesting again that this star’s metallicity is similar to that of the SMC. However, the SMC stars have measured C III 1176 Å EWs that scatter to lower values than TLUSTY models would predict for their reported T_{eff} and $\log(g) \geq 4.0$ (Bouret et al. 2013). This is perhaps unsurprising, as their properties were determined using CMFGEN models that fit for many parameters that are fixed in the OSTAR2002 grid, like metal abundance ratios and microturbulence.

Figure 8 demonstrates that the dependence of C III 1176 Å EW on T_{eff} is stronger than that on $\log(g)$ or Z , at least when restricted to $Z \leq 20\% Z_{\odot}$. The EWs of the coolest target star, S3, and its SMC analogs are all offset to higher values than those of the hotter stars, despite the range in Z sampled. This raises the possibility that C III 1176 Å EW can be used to probe the stellar population temperature and therefore age of metal-poor galaxies. We suggest that C III 1176 Å EWs should be explored as a tool to analyze the stellar populations of low- Z galaxies in the nearby universe.

4.2. Comparison to Previous Work on the Target Stars and Their Host Galaxies

Here, we discuss our results in the context of previous studies of the target stars and of other massive stars in the same host galaxies. Optical spectra exist for all three stars, though their resolution and/or SNR is generally not high enough for reliable determination of stellar

properties. We compare our estimates of stellar properties with expectations based on existing data.

LP26—This star was identified as the lone O star in Leo P in optical *HST* photometry (McQuinn et al. 2015b) and was later confirmed to show He II absorption indicative of an O-type star in $R \sim 2000$ optical spectroscopy (Evans et al. 2019). LP26 is powering the only H II region in the galaxy, and spectroscopic observations therefore sample both the stellar and nebular flux. Strong nebular He I emission precludes a detailed analysis of the optical spectrum, so its spectral type can only be estimated. This is made difficult by the lack of an empirical calibration between bolometric correction and spectral type at very low Z ; the fraction of the L_\star of a given O type emitted in the optical should decrease with decreasing metallicity, as T_{eff} shifts higher for fixed spectral type. McQuinn et al. (2015b) argued based on expectations for Galactic O stars that the absolute V -band magnitude of LP26 suggests an O5 V type, or possibly two blended O7-8 V stars each with $M_\star \sim 25 M_\odot$. Our SED analysis here prefers a $22 M_\odot$ star with $T_{\text{eff}} \sim 37.5$ kK, the latter being consistent with O7 V stars in the SMC (Ramachandran et al. 2019). We find no indications of a binary companion and do not model the star as an unresolved binary, yet our results agree with previous estimates of LP26’s properties based on the assumption that it is an unresolved binary. This can potentially be explained by accounting for the very low Z of LP26 in our SED modeling, and/or the inclusion of FUV and NIR data in this analysis providing more information than the optical photometry alone.

S3—Garcia et al. (2019) identified four O-dwarf stars in the outskirts of Sextans A, including S3 (and two ULLYSES Targets, S2 and S4). They used $R \sim 1000$ spectra to assign the spectral type O9 V and compared S3’s extinction-corrected position on a ground-based optical CMD with stellar evolution tracks from Lejeune & Schaerer (2001). That comparison suggested $M_\star \sim 25 - 40 M_\odot$ and an age of $\sim 1.5 - 6.3$ Myr. The present analysis assumes different distance, foreground extinction, and adopted stellar evolution models, yet paints a remarkably consistent picture given these many uncertain factors. Our SED modeling, including FUV and NIR constraints, prefers a slightly lower-mass and more evolved star ($M_\star \sim 21 M_\odot$, age ~ 9 Myr), but roughly agrees within the uncertainties reported here and in Garcia et al. (2019). The best-fit SED model agrees with the FUV photospheric features (Figure 6), but many informative diagnostic lines are undetected due to relatively low SNR combined with high $v \sin(i)$.

Garcia et al. (2017) presented a low-resolution ($R \sim 2600$) *HST*/COS spectrum of an O7.5 III star in Sextans A. Compared to similar spectral type stars in IC 1613 and the SMC, the photospheric metal lines and wind features appear substantially weaker in the Sextans A star, indicating a substantially lower metal content than $20\% Z_\odot$. This is consistent with our SED analysis, which prefers a low $Z \sim 0.00056$ ($1/30 Z_\odot$ in the OSTAR2002 grid, or $4\% Z_\odot$ relative to $Z_\odot = 0.0142$; Asplund et al. 2009). O stars in Sextans A are thus important targets for future observational efforts to constrain the astrophysics of stars more metal-poor than the SMC.

A15—Bresolin et al. (2006) presented the $R \sim 900$ optical spectrum and determined the O7 V((f)) spectral type for this star, but deemed the SNR of the data too low for parameter inference. No estimates of its properties exist in the literature to the best of our knowledge.

Another O-type star (A11, O9.7 Ia) in WLM has been analyzed in detail by Tramper et al. (2014) and Bouret et al. (2015). The latter authors obtained *HST*/COS FUV data to complement its optical spectrum and fit CMFGEN models to infer wind and stellar properties, including detailed abundances. They found an SMC-like stellar Fe abundance of 20% solar, though could not rule out a lower value of 14% solar given the SNR of the data. Based on our SED analysis of A15 and comparison to analog stars in the SMC, we argue that A15 may also have SMC-like metal abundances, consistent with the only other O star in WLM observed in the FUV. Together, these results suggest that WLM, like IC 1613 (Garcia et al. 2014; Bouret et al. 2015), is not substantially more metal-poor (if at all) than the SMC, and may have subsolar α/Fe .

4.3. Implications for Low- Z Stellar Populations

We have analyzed the first FUV spectra of mid-late O V stars in metal-poor galaxies. Though a sample of three is obviously small, these data represent an important step toward empirical constraints on the purely theoretical spectral and evolution models that are used to model stellar populations at low Z . Here we compare our findings to the theoretical expectations that underlie the current generation of SPS models.

4.3.1. Stellar Winds

Radiation-driven mass loss is theoretically expected to weaken with decreasing metallicity due to the lower opacity of the photospheric metal lines that transfer momentum to stellar winds (e.g., Castor et al. 1975; Abbott 1982; Vink et al. 2001). While this general expectation has been validated with observations down to the

20% Z_{\odot} population of massive stars in the SMC, the precise scaling of \dot{M}_{\star} with Z remains unclear (Mokiem et al. 2007; Ramachandran et al. 2019; Björklund et al. 2021). The picture becomes even murkier at lower Z due to the lack of spectroscopic observations of individual metal-poor O stars in galaxies more distant than the Magellanic Clouds. Tramper et al. (2011, 2014) reported higher \dot{M}_{\star} than expected from radiation-driven wind theory based on analysis of optical spectra of several O stars in the metal-poor galaxies WLM, IC 1613, and NGC 3109, but later modeling of the wind profiles in FUV spectra of three of those stars by Bouret et al. (2015) found lower \dot{M}_{\star} . Furthermore, the O stars in two of those galaxies with gas-phase oxygen abundances below 20% Z_{\odot} appear to have SMC-like Fe abundances (Garcia et al. 2014; Bouret et al. 2015), alleviating the apparent tension between observations and theory. The challenge of identifying stars with Fe abundances below 20% Z_{\odot} , even in galaxies with nebular oxygen abundances below that threshold, remains a limiting factor in our understanding of stellar winds at low Z .

More distant dwarf irregulars with gas-phase oxygen abundances below 10% Z_{\odot} are the new observational frontier. Ten O stars have been spectroscopically confirmed in the very metal-poor galaxies Sextans A (6% Z_{\odot} ; Camacho et al. 2016; Garcia et al. 2019) and Leo P (3% Z_{\odot} ; Evans et al. 2019), but their FUV properties have yet to be analyzed in detail. The low-resolution COS spectrum of an O giant in Sextans A presented by Garcia et al. (2017) revealed weak metal absorption and wind features relative to similar stars in IC 1613 and the SMC, suggesting that it is substantially more metal-poor than 20% Z_{\odot} . Our analysis of S3 in Sextans A and LP26 in Leo P agrees with this picture. Their FUV spectra show weak photospheric metal lines, particularly in Fe forest regions, though this appears to be partly due to high $v \sin(i)$ broadening the features to the extent that they cannot be detected over the noise level of the continuum. The SED modeling in Section 3.4 prefers $Z < 5\% Z_{\odot}$ for both LP26 and S3, and the best-fit models reproduce the photospheric absorption features in their FUV spectra remarkably well. These results, combined with the comparison to SMC stars in Figure 7, indicate that these stars are indeed significantly more metal-poor than the SMC, opening a new window onto the astrophysics of massive stars at extremely low Z .

Qualitatively, the FUV spectra of S3 and LP26 are consistent with recent theoretical work at 1/30 Z_{\odot} . Martins & Palacios (2021) predict that low mass-loss winds driven by extremely low- Z stars on the main sequence result in weak wind profiles that only show absorp-

tion, using the Vink et al. (2001) mass-loss prescription with reduced normalization to account for the effects of clumping. Observations agree with their predicted spectra: no wind emission or well-developed P-Cygni profiles are seen in our *HST*/COS spectra of S3 and LP26 (Section 3.2), or in the spectrum of the O7.5 III Sextans A star presented in Garcia et al. (2017). Detailed modeling of the photospheric and wind transitions to constrain the abundances and \dot{M}_{\star} of these extremely metal-poor stars is beyond the scope of this paper, but such analysis and comparison to quantitative mass-loss prescriptions in the literature will be the subject of future work.

The behavior of \dot{M}_{\star} at low Z has important implications for ionizing photon production, both in nearby dwarf galaxies and in the early universe. Not only does the wind strength affect a star’s lifetime and surface properties, it also determines the opacity to ionizing photons, particularly those capable of ionizing He II (Schaerer & de Koter 1997; Martins & Palacios 2021). However, different modeling approaches find different \dot{M}_{\star} normalization and scaling with metallicity (e.g., Vink et al. 2001; Krtićka & Kubát 2017; Bestenlehner 2020; Vink & Sander 2021). Since most widely-used stellar evolution and SPS models adopt the same Vink et al. (2001) mass-loss prescription, which seems to over-predict \dot{M}_{\star} relative to empirical studies in the SMC (Ramachandran et al. 2019; Björklund et al. 2021), it is possible that stellar evolution is being modeled incorrectly at low Z . Future work to constrain \dot{M}_{\star} for metal-poor stars, including new observations to expand the current small sample, is urgently needed to anchor models of low- Z stellar populations. This could help to alleviate the discrepancy between current SPS models and the hard ionizing spectra implied by nebular emission in nearby dwarf galaxies (e.g., Berg et al. 2019; Senchyna et al. 2019) and will help to determine the dominant ionizing photon producers during cosmic reionization.

It is interesting that only one of the three stars in our sample, LP26, powers a strong H II region. This star does not appear to be substantially hotter or more massive than the others, yet it is the most metal-poor and has the weakest wind features of the three. The appearance of the H II region in Leo P could be related to its low star formation rate ($2.1 \times 10^{-5} M_{\odot} \text{ yr}^{-1}$; McQuinn et al. 2015b): if few massive stars capable of clearing out neutral gas have formed close to LP26 in the recent past, we would expect a high local density of neutral gas to be available for LP26 to ionize. Yet the fact that LP26 powers strong nebular emission despite its modest inferred T_{eff} of 37.5 kK suggests that this metal-poor star with weak winds has a relatively large ionizing flux. In future work, we will use the H II region emission pow-

ered by LP26 to constrain its ionizing spectrum and shed light on whether weak winds can lead to the production of enough energetic photons to explain the extreme nebular emission seen in very low- Z galaxies.

4.3.2. Rotation

Stellar rotation affects the surface properties, chemical mixing, lifetimes, and ionizing photon production of massive stars. A wide range of $v \sin(i)$ is observed, and stars do not maintain the same rotation speed throughout their evolution. Angular momentum loss via stellar winds is expected to slow a massive star’s rotation over its lifetime, though other mechanisms like magnetic braking may also play a role. As mass loss is expected to weaken with decreasing metallicity, winds should become less efficient at reducing surface rotation in metal-poor stars.

Observations of large samples of OB stars in the Milky Way and Magellanic Clouds have probed the effects of stellar age, evolutionary status, Z , and environment on the distribution of $v \sin(i)$. Across all three galaxies, OB stars appear to follow a bimodal $v \sin(i)$ distribution with most stars populating a relatively low-velocity peak and a smaller fraction forming a long tail to high $v \sin(i)$, reaching up to $\sim 600 \text{ km s}^{-1}$ in the LMC (e.g., Ramírez-Agudelo et al. 2013; Ramachandran et al. 2019). The tail of fast rotators is thought to be produced by binary interactions, with secondaries spun up by mass transfer, which may be more efficient at low Z (de Mink et al. 2013). Interestingly, a recent compilation by Ramachandran et al. (2019) showed that the peak of the low-velocity part of the $v \sin(i)$ distributions shifts higher with decreasing metallicity, as does the fraction of OB stars populating the high-velocity tail ($v \sin(i) \geq 200 \text{ km s}^{-1}$).

We found that the two lower- Z O dwarfs in our sample, both in galaxies with nebular oxygen abundances $\leq 6\% Z_{\odot}$, have $v \sin(i) \geq 290 \text{ km s}^{-1}$ (Section 3.3). These are the highest reported $v \sin(i)$ of O stars in galaxies more metal-poor than the SMC, which is striking because rotation or line widths were not used in sample selection. Broadening measurements, giving an upper limit on $v \sin(i)$, were reported for a handful of O stars in WLM, IC 1613, and NGC 3109, spanning a fairly broad distribution with typical values $\sim 100 \text{ km s}^{-1}$ (Tramper et al. 2011, 2014; Garcia et al. 2014). However, none of these galaxies has been demonstrated to host O stars that have lower Fe abundances than $20\% Z_{\odot}$. The only other $v \sin(i)$ measurements for stars that are securely below SMC metallicity were recently reported by Ramachandran et al. (2021), who analyzed three O stars in the $\sim 10\% Z_{\odot}$ Magellanic Bridge, tidal debris from

past interaction between the LMC and SMC. Curiously, two out of the three stars in that sample were found to be extremely narrow-lined slow rotators, with $v \sin(i)$ less than 10 km s^{-1} . Both stars appear to have binary companions, and the authors suggest the slow rotation may be due to tidal locking. Our $v \sin(i)$ measurements for LP26 and S3 appear to be the first constraints on how stellar rotation operates in (apparently) single extremely metal-poor O stars. While it is possible that our target stars have binary companions, the data are entirely consistent with them being single stars and companions are not required to explain our observations.

Figure 9 compares the $v \sin(i)$ we measure for our metal-poor sample to the distribution of $v \sin(i)$ observed for O dwarfs in the SMC. The colored lines show three cumulative distributions of $v \sin(i)$ measured for SMC O dwarfs (defined as luminosity class IV and V here) using different samples, data, and measurement techniques (Penny & Gies 2009; Bouret et al. 2013; Ramachandran et al. 2019). These samples contain between 12 and 23 stars. We indicate the $v \sin(i)$ measured for our three target stars as vertical black lines, where A15 is shown as a dotted line to clarify that it appears to be similar in Z to the SMC sample, while the substantially more metal-poor LP26 and S3 are shown as solid lines. The fraction of stars in the SMC distributions that have lower $v \sin(i)$ than a given value can be read off from this plot as the y-axis value corresponding to that $v \sin(i)$. A15’s $v \sin(i)$ is larger than that of $\sim 35 - 60\%$ of the SMC stars, placing it close to the median of the $v \sin(i)$ distribution for SMC O dwarfs. In contrast, both LP26 and S3 have $v \sin(i)$ that is higher than 90% of the SMC distribution. This is strongly suggestive that the rotation speeds of extremely metal-poor O dwarfs ($< 10\% Z_{\odot}$) are drawn from a different distribution than that of similar stars in the SMC, in the sense that very metal-poor stars may typically rotate faster.

How likely would it be to find that two out of our three metal-poor stars are fast rotators if their $v \sin(i)$ distribution is the same as that of SMC O dwarfs? Taking 290 km s^{-1} (the $v \sin(i)$ of S3) as the lower limit, Figure 9 shows there is a 10% chance that SMC stars rotate faster than that. We can use the binomial distribution to calculate the probability of successes in two out of three trials given a 10% chance of success on independent trials:

$$\Pr(k | n, p) = \frac{n!}{k!(n-k)!} p^k (1-p)^{n-k}, \quad (4)$$

where $k = 2$, $n = 3$, and $p = 0.1$. This gives just a 3% chance of finding such high $v \sin(i)$ for two of our targets if very metal-poor stars do have a similar $v \sin(i)$

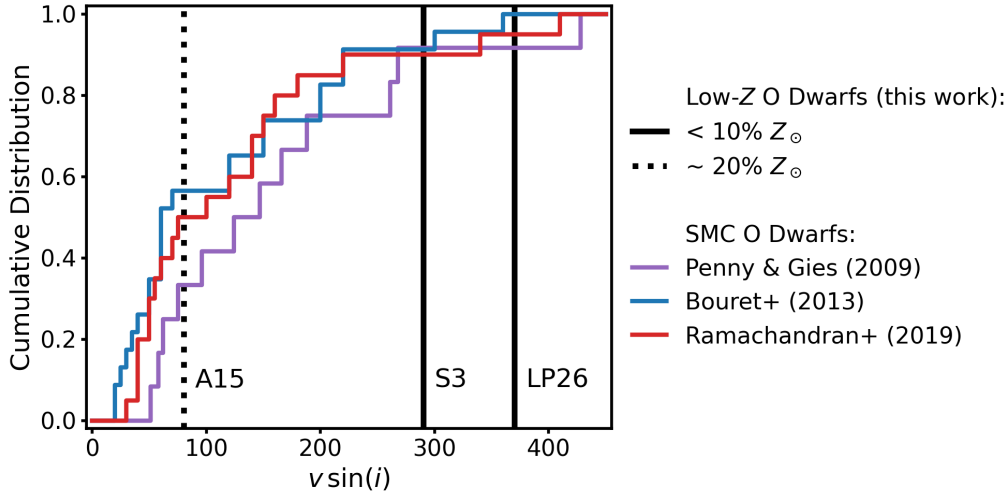


Figure 9. Both extremely metal-poor stars have $v \sin(i)$ similar to the fastest-rotating SMC O dwarfs. The cumulative distribution of $v \sin(i)$ measured for three samples of O dwarfs in the SMC using different data and methods are plotted as colored lines (Penny & Gies 2009; Bouret et al. 2013; Ramachandran et al. 2019). The $v \sin(i)$ we measure for our three metal-poor O dwarfs are indicated with black vertical lines. A15, which seems to have similar Z to SMC stars, is shown as a dashed line, while the two stars that appear to be substantially metal-poorer, LP26 and S3, are shown as solid lines. While the $v \sin(i)$ of A15 falls near the median of these distributions (cumulative probability of 35-60%), both LP26 and S3 have $v \sin(i)$ higher than 90% of the measurements for SMC O dwarfs. Given that these were not selected to be fast rotators, this comparison suggests that the rotation speeds of very metal-poor O stars are different than the distribution observed in the SMC.

distribution to that in the SMC. However, we have argued that A15 has a relatively high Z similar to SMC stars, so it may not be fair to count that star as being metal-poor. We repeat the above exercise with the following modifications: (1) we adopt the lowest $v \sin(i)$ allowed within the uncertainties for the two very metal-poor stars, 200 km s^{-1} (Section 3.3), as a more conservative threshold, and (2) we calculate the probability of finding that two out of two very metal-poor O stars are fast rotators by this new definition. 200 km s^{-1} is larger than $\sim 75 - 85\%$ of the $v \sin(i)$ measured for SMC O dwarfs, so we adopt a conservatively high 25% chance of success per trial. With $k = 2$, $n = 2$, and $p = 0.25$, we find a 6% probability that metal-poor O dwarfs have the same $v \sin(i)$ distribution as their SMC counterparts. While our sample size is obviously small, this exercise strongly suggests that extremely metal-poor O stars typically rotate faster than higher- Z stars in the SMC.

It is interesting to compare these high $v \sin(i)$ to the rotation speeds at which the stars would break apart. Using the M_* and R_* inferred from the best-fit SED models for each star (Section 3.4), we can estimate their critical rotation speeds as:

$$v_{\text{crit}} = \left(\frac{GM_*}{R_*} \right)^{1/2}. \quad (5)$$

For simplicity, we use the R_* inferred from non-rotating evolution models, but in detail, fast-rotating stars are nonspherical. The equatorial radius is 1.5 times the po-

lar radius at critical rotation, which would drive v_{crit} lower, so our simple calculation gives a conservatively high estimate of v_{crit} . We find that $v \sin(i)$ measured for LP26 and S3 are 52% and 50% of their v_{crit} , comparable to but slightly higher than the 40% v_{crit} often adopted in rotating evolutionary models (e.g., Geneva and MIST; Ekström et al. 2012; Choi et al. 2016). A15’s measured $v \sin(i)$ is about 10% v_{crit} .

The best-fit SED models favor ages of at least several Myr for all three stars in our sample, suggesting that all of these low- Z O dwarfs have progressed through a large part of their main-sequence lifetimes. S3 appears to be the most evolved of the three, with a best-fit age of 9 Myr. The high $v \sin(i)$ of LP26 and S3 suggest that either these stars have maintained high rotation rates throughout a large fraction of their main-sequence lifetimes, or potentially could be the spun-up remnants of mass transfer from a former binary companion (de Mink et al. 2013). Neither star shows strong wind absorption profiles (Section 3.2), so their stellar winds must be optically thin and therefore removing little mass and angular momentum from the stars. Our findings are consistent with the expectation that metal-poor massive stars spin down less than their higher- Z counterparts (e.g., Meynet & Maeder 2002; Brott et al. 2011; Groh et al. 2019), though it is impossible to differentiate between this possibility and potential binary interactions.

Trends between $v \sin(i)$ of OB stars and their environments may provide a clue. Specifically, the rapidly ro-

tating tail of the $v \sin(i)$ distribution is more populated in the field of the LMC compared to clusters (Ramírez-Agudelo et al. 2013). The reason for this is not clear, but could be explained if spun-up secondaries are frequently ejected from their natal clusters by the supernovae of the shorter-lived primaries. In such a scenario, we would expect to find a correlation between the $v \sin(i)$ of field stars and large radial velocity offsets from the galaxy systemic velocity. As reported in Table 6, we find no large v_{radial} discrepancies between our target stars and their host galaxies that would suggest they had been kicked by a companion star’s supernova.

Our findings suggest that rotation is important to include in stellar evolution and SPS models at low Z . Rotation can boost ionizing photon production by massive stars (e.g., Szécsi et al. 2015; Topping & Shull 2015; Murphy et al. 2021), and so is important to include in modeling of the metal-poor stellar populations that power nebular emission in local dwarf galaxies and contributed to the reionization of the universe. But the small number of $v \sin(i)$ measurements at low Z limits our ability to draw broad conclusions. Future observational efforts should aim to obtain moderate-resolution spectra of more O-type stars in nearby, metal-poor galaxies from which $v \sin(i)$ can be constrained. Only with a statistical sample spanning a range of spectral types and luminosity classes can we determine whether the apparent trend for lower- Z stars to maintain higher rotation speeds over their main-sequence lifetimes is real.

5. CONCLUSIONS

We have presented new medium-resolution *HST*/COS FUV spectra of the metal-poor O V stars LP26, S3, and A15, residing in nearby dwarf galaxies spanning 3–14% Z_{\odot} . From these data, we measured the strengths of their photospheric and wind lines and constrained their projected rotation speeds from the structure of the C III 1176 Å feature. We combined the FUV spectra with NUV, optical, and NIR *HST* photometry and modeled the SEDs to estimate key stellar parameters, including T_{eff} , $\log(g)$, M_{\star} , L_{\star} , and age. Finally, we compared the observed FUV spectra of the metal-poor O dwarfs to those of stars with similar properties in the 20% Z_{\odot} SMC to assess empirically the impact of Z on FUV spectral properties. Our conclusions are:

1. Many photospheric metal lines are clearly detected in the highest- Z star, A15, but the stellar continua are strikingly featureless in the two very low- Z stars, LP26 and S3. This is likely due to a combination of intrinsically weak lines and broadening due to high $v \sin(i)$. We measure equivalent widths

of the photospheric lines as a benchmark for models at low Z (Section 3.1, Figure 2, Table 4).

2. The most metal-poor star, LP26, has no clear wind features, while S3 shows under-developed C IV 1550 Å wind absorption that likely arises only in the inner, denser part of the wind. A15 has two well-developed (though unstaured) wind profiles that suggest $v_{\infty} \gtrsim 1400 \text{ km s}^{-1}$, similar to measurements for mid-late O stars in the SMC (Section 3.2, Figure 3, Table 5).
3. The two extremely low- Z stars, LP26 and S3, have $v \sin(i) \geq 290 \text{ km s}^{-1}$, supporting the expectation that angular momentum loss via stellar winds becomes less efficient with decreasing metallicity. The high rotation speeds broaden weak photospheric lines such that they cannot be detected above the noise in the FUV spectra. A15, on the other hand, has a relatively low $v \sin(i)$ of 80 km s^{-1} (Section 3.3, Figure 4, Table 6).
4. We estimate just a 3 – 6% probability of finding that both LP26 and S3 have such high $v \sin(i)$ if they are drawn from the same $v \sin(i)$ distribution as observed in the SMC. This strongly suggests that we should expect the population of extremely metal-poor massive stars ($< 10\% Z_{\odot}$) to have higher typical rotation speeds than more metal-rich populations (Section 4.3.2, Figure 9).
5. The best-fit SED models suggest that all three of our targets are relatively low-mass ($M_{\star} \lesssim 30 M_{\odot}$) O stars that have evolved through a substantial fraction of their main-sequence lifetimes (ages of $\sim 4 - 9 \text{ Myr}$; Section 3.4, Figure 5, Table 7). We compare the the best-fit model predictions of photospheric line profiles and continuum levels in the FUV to the observed COS spectra and find excellent agreement overall, supporting our inferred stellar properties and validating the use of the theoretical OSTAR2002 atmosphere grid down to very low Z (Figure 6).
6. We compare FUV spectra of the three metal-poor O stars to analogs in the SMC, controlling for the effects of all stellar properties except Z . A15 shows photospheric and wind features at least as strong as those in its SMC analog stars, suggesting that its stellar Z may be higher than the gas-phase oxygen abundance of WLM. Only the most metal-poor star, LP26, has obviously weaker wind lines than its SMC analogs, supporting the expectation of lower \dot{M}_{\star} with decreasing metallicity

(Section 4.1, Figure 7). Both LP26 and S3 have smaller C III 1176 Å EWs than their SMC analogs, while A15’s is intermediate between its comparison stars. We suggest that C III 1176 Å EW may be a useful age diagnostic for unresolved massive stellar populations at low Z (Figure 8).

These results provide a new window into the astrophysics of extremely metal-poor O-dwarf stars. Though the sample size is small, this work demonstrates that FUV spectra of individual massive stars contain a wealth of information and can be used to anchor theoretical stellar evolution and atmosphere models upon which our understanding of the ionizing flux and feedback of metal-poor stellar populations depend. In the future, we will fit detailed stellar atmosphere models to the FUV and optical spectra of these metal-poor O dwarfs to quantify the abundances of individual metals and constrain the wind properties, particularly \dot{M}_* and v_∞ . The inferred stellar and wind properties will enable a unique test of mass-loss models below 20% Z_\odot , and the atmosphere models will enable a data-driven estimate of the ionizing flux from metal-poor O stars.

OGT thanks Ben Williams and Karl Gordon for helpful discussions and Max Newman for contributions to the photometry pipeline used in this work.

This work was supported by the Space Telescope Science Institute through GO-15967. OGT was also supported by Rutgers University. This work is based on observations made with the NASA/ESA *Hubble Space Telescope*, obtained from the data archive at the Space Telescope Science Institute. STScI is operated by the Association of Universities for Research in Astronomy, Inc. under NASA contract NAS 5-26555. This work was performed in part at Aspen Center for Physics, which is supported by National Science Foundation grant PHY-1607611. This work was partially supported by a grant from the Simons Foundation.

This research has extensively used NASA’s Astrophysics Data System, *adstex*⁵, and the arXiv preprint server. The Digitized Sky Survey was produced at the Space Telescope Science Institute under U.S. Government grant NAG W-2166. The images of these surveys are based on photographic data obtained using the Oschin Schmidt Telescope on Palomar Mountain and the UK Schmidt Telescope. The plates were processed into the present compressed digital form with the permission of these institutions.

Software: *Astrodrizzle* (Gonzaga et al. 2012), *Astropy* (Astropy Collaboration et al. 2013, 2018), *BEAST* (Gordon et al. 2016), *DOLPHOT* (Dolphin 2000, 2016), *HDF5* (The HDF Group 1997-2020), *iPython* (Perez & Granger 2007), *Matplotlib* (Hunter 2007), *NumPy* (Harris et al. 2020), *SAOImageDS9* (Joye & Mandel 2003), *SciPy* (Virtanen et al. 2020)

APPENDIX

A. CONTINUUM NORMALIZATION

Table A1 reports the spectral bandpasses used to fit the local continuum level for each spectral line analyzed in this paper. We selected a narrow range of wavelengths on either side of the spectral line, ensuring that the continuum regions were free of both ISM lines and strong photospheric lines. To ensure that we weren’t missing photospheric absorption masked by the noise in the continuum, we used *TLUSTY* spectra to check for predicted metal absorption in all of the bandpasses we used. For most lines, we modeled the local continuum with a simple linear fit to the spectrum in the blue and red bandpasses, and visually inspected all fits and normalized spectra to confirm that this procedure produced good results. The N v 1238, 1242 Å feature was the only case where a linear fit did not perform well because this spectral region is affected by the wing of the Lyman α absorption profile. For that line only, we modeled the continuum with a third-order polynomial to capture the more complex structure. The same continuum bandpasses were used for all three stars.

REFERENCES

- Abbott, D. C. 1982, *ApJ*, 259, 282, doi: [10.1086/160166](https://doi.org/10.1086/160166)
- Asplund, M., Grevesse, N., Sauval, A. J., & Scott, P. 2009, *ARA&A*, 47, 481, doi: [10.1146/annurev.astro.46.060407.145222](https://doi.org/10.1146/annurev.astro.46.060407.145222)
- Astropy Collaboration, Robitaille, T. P., Tollerud, E. J., et al. 2013, *A&A*, 558, A33, doi: [10.1051/0004-6361/201322068](https://doi.org/10.1051/0004-6361/201322068)

⁵ <https://github.com/yymao/adstex>

Table A1. Bandpasses Used for Continuum Normalization

Feature	Blue Continuum Bandpass (Å)	Red Continuum Bandpass (Å)
C III 1176	1171.0 – 1173.5	1177.5 – 1181.5
N III 1184	1179.8 – 1181.2	1186.5 – 1187.2
N V 1238, 1242	1229.0 – 1232.7	1248.5 – 1256.5
C III 1247	1245.0 – 1246.4	1248.0 – 1249.0
O IV 1341	1328.5 – 1332.0	1345.0 – 1350.0
Fe V/C III 1428	1423.0 – 1425.0	1433.3 – 1434.8
Fe V 1445	1433.3 – 1434.7	1457.0 – 1458.3
S V 1502	1497.0 – 1500.0	1505.0 – 1508.0
C IV 1548, 1550	1535.0 – 1536.3	1565.0 – 1565.5
Fe IV 1570	1558.0 – 1559.5	1580.5 – 1582.3
He II 1640	1633.0 – 1636.5	1644.5 – 1646.5
N IV 1718	1709.0 – 1714.0	1725.0 – 1729.0

- Astropy Collaboration, Price-Whelan, A. M., Sipőcz, B. M., et al. 2018, *AJ*, 156, 123, doi: [10.3847/1538-3881/aabc4f](https://doi.org/10.3847/1538-3881/aabc4f)
- Becker, R. H., Fan, X., White, R. L., et al. 2001, *AJ*, 122, 2850, doi: [10.1086/324231](https://doi.org/10.1086/324231)
- Berg, D. A., Chisholm, J., Erb, D. K., et al. 2019, *ApJL*, 878, L3, doi: [10.3847/2041-8213/ab21dc](https://doi.org/10.3847/2041-8213/ab21dc)
- Berg, D. A., Erb, D. K., Auger, M. W., Pettini, M., & Brammer, G. B. 2018, *ApJ*, 859, 164, doi: [10.3847/1538-4357/aab7fa](https://doi.org/10.3847/1538-4357/aab7fa)
- Bestenlehner, J. M. 2020, *MNRAS*, 493, 3938, doi: [10.1093/mnras/staa474](https://doi.org/10.1093/mnras/staa474)
- Björklund, R., Sundqvist, J. O., Puls, J., & Najarro, F. 2021, *A&A*, 648, A36, doi: [10.1051/0004-6361/202038384](https://doi.org/10.1051/0004-6361/202038384)
- Bouret, J. C., Lanz, T., Hillier, D. J., et al. 2015, *MNRAS*, 449, 1545, doi: [10.1093/mnras/stv379](https://doi.org/10.1093/mnras/stv379)
- Bouret, J. C., Lanz, T., Martins, F., et al. 2013, *A&A*, 555, A1, doi: [10.1051/0004-6361/201220798](https://doi.org/10.1051/0004-6361/201220798)
- Bresolin, F., Pietrzyński, G., Urbaneja, M. A., et al. 2006, *ApJ*, 648, 1007, doi: [10.1086/506200](https://doi.org/10.1086/506200)
- Bressan, A., Marigo, P., Girardi, L., et al. 2012, *MNRAS*, 427, 127, doi: [10.1111/j.1365-2966.2012.21948.x](https://doi.org/10.1111/j.1365-2966.2012.21948.x)
- Brott, I., de Mink, S. E., Cantiello, M., et al. 2011, *A&A*, 530, A115, doi: [10.1051/0004-6361/201016113](https://doi.org/10.1051/0004-6361/201016113)
- Byler, N., Dalcanton, J. J., Conroy, C., & Johnson, B. D. 2017, *ApJ*, 840, 44, doi: [10.3847/1538-4357/aa6c66](https://doi.org/10.3847/1538-4357/aa6c66)
- Camacho, I., Garcia, M., Herrero, A., & Simón-Díaz, S. 2016, *A&A*, 585, A82, doi: [10.1051/0004-6361/201425533](https://doi.org/10.1051/0004-6361/201425533)
- Cardelli, J. A., Clayton, G. C., & Mathis, J. S. 1989, *ApJ*, 345, 245, doi: [10.1086/167900](https://doi.org/10.1086/167900)
- Castor, J. I., Abbott, D. C., & Klein, R. I. 1975, *ApJ*, 195, 157, doi: [10.1086/153315](https://doi.org/10.1086/153315)
- Chisholm, J., Rigby, J. R., Bayliss, M., et al. 2019, *ApJ*, 882, 182, doi: [10.3847/1538-4357/ab3104](https://doi.org/10.3847/1538-4357/ab3104)
- Choi, J., Dotter, A., Conroy, C., et al. 2016, *ApJ*, 823, 102, doi: [10.3847/0004-637X/823/2/102](https://doi.org/10.3847/0004-637X/823/2/102)
- Conroy, C. 2013, *ARA&A*, 51, 393, doi: [10.1146/annurev-astro-082812-141017](https://doi.org/10.1146/annurev-astro-082812-141017)
- Conroy, C., Gunn, J. E., & White, M. 2009, *ApJ*, 699, 486, doi: [10.1088/0004-637X/699/1/486](https://doi.org/10.1088/0004-637X/699/1/486)
- Crowther, P. A., Caballero-Nieves, S. M., Bostroem, K. A., et al. 2016, *MNRAS*, 458, 624, doi: [10.1093/mnras/stw273](https://doi.org/10.1093/mnras/stw273)
- Dalcanton, J. J., Williams, B. F., Seth, A. C., et al. 2009, *ApJS*, 183, 67, doi: [10.1088/0067-0049/183/1/67](https://doi.org/10.1088/0067-0049/183/1/67)
- de Koter, A., Heap, S. R., & Hubeny, I. 1998, *ApJ*, 509, 879, doi: [10.1086/306503](https://doi.org/10.1086/306503)
- de Mink, S. E., Langer, N., Izzard, R. G., Sana, H., & de Koter, A. 2013, *ApJ*, 764, 166, doi: [10.1088/0004-637X/764/2/166](https://doi.org/10.1088/0004-637X/764/2/166)
- Dolphin, A. 2016, *DOLPHOT: Stellar photometry*. <http://ascl.net/1608.013>
- Dolphin, A. E. 2000, *PASP*, 112, 1383, doi: [10.1086/316630](https://doi.org/10.1086/316630)
- Doran, E. I., Crowther, P. A., de Koter, A., et al. 2013, *A&A*, 558, A134, doi: [10.1051/0004-6361/201321824](https://doi.org/10.1051/0004-6361/201321824)
- Dorn-Wallenstein, T. Z., & Levesque, E. M. 2020, *ApJ*, 896, 164, doi: [10.3847/1538-4357/ab8d28](https://doi.org/10.3847/1538-4357/ab8d28)
- Dufour, R. J. 1984, in *Structure and Evolution of the Magellanic Clouds*, ed. S. van den Bergh & K. S. D. de Boer, Vol. 108, 353–361, doi: [10.1017/S0074180900040481](https://doi.org/10.1017/S0074180900040481)
- Ekström, S., Georgy, C., Eggenberger, P., et al. 2012, *A&A*, 537, A146, doi: [10.1051/0004-6361/201117751](https://doi.org/10.1051/0004-6361/201117751)
- Eldridge, J. J., Stanway, E. R., Xiao, L., et al. 2017, *PASA*, 34, e058, doi: [10.1017/pasa.2017.51](https://doi.org/10.1017/pasa.2017.51)
- Emerick, A., Bryan, G. L., & Mac Low, M.-M. 2019, *MNRAS*, 482, 1304, doi: [10.1093/mnras/sty2689](https://doi.org/10.1093/mnras/sty2689)

- Evans, C. J., Castro, N., Gonzalez, O. A., et al. 2019, *A&A*, 622, A129, doi: [10.1051/0004-6361/201834145](https://doi.org/10.1051/0004-6361/201834145)
- Finkelstein, S. L., D’Aloisio, A., Paardekooper, J.-P., et al. 2019, *ApJ*, 879, 36, doi: [10.3847/1538-4357/ab1ea8](https://doi.org/10.3847/1538-4357/ab1ea8)
- Fitzpatrick, E. L. 1999, *PASP*, 111, 63, doi: [10.1086/316293](https://doi.org/10.1086/316293)
- Garcia, M., Herrero, A., Najarro, F., et al. 2017, in *The Lives and Death-Throes of Massive Stars*, ed. J. J. Eldridge, J. C. Bray, L. A. S. McClelland, & L. Xiao, Vol. 329, 313–321, doi: [10.1017/S1743921317003088](https://doi.org/10.1017/S1743921317003088)
- Garcia, M., Herrero, A., Najarro, F., Camacho, I., & Lorenzo, M. 2019, *MNRAS*, 484, 422, doi: [10.1093/mnras/sty3503](https://doi.org/10.1093/mnras/sty3503)
- Garcia, M., Herrero, A., Najarro, F., Lennon, D. J., & Alejandro Urbaneja, M. 2014, *ApJ*, 788, 64, doi: [10.1088/0004-637X/788/1/64](https://doi.org/10.1088/0004-637X/788/1/64)
- Gonzaga, S., Hack, W., Fruchter, A., & Mack, J. 2012, *The DrizzlePac Handbook*
- Gordon, K. D., Clayton, G. C., Misselt, K. A., Landolt, A. U., & Wolff, M. J. 2003, *ApJ*, 594, 279, doi: [10.1086/376774](https://doi.org/10.1086/376774)
- Gordon, K. D., Fouesneau, M., Arab, H., et al. 2016, *ApJ*, 826, 104, doi: [10.3847/0004-637X/826/2/104](https://doi.org/10.3847/0004-637X/826/2/104)
- Götberg, Y., de Mink, S. E., Groh, J. H., Leitherer, C., & Norman, C. 2019, *A&A*, 629, A134, doi: [10.1051/0004-6361/201834525](https://doi.org/10.1051/0004-6361/201834525)
- Gray, D. F. 1976, *The observation and analysis of stellar photospheres*
- . 1992, *The observation and analysis of stellar photospheres.*, Vol. 20
- Green, G. M., Schlafly, E. F., Finkbeiner, D. P., et al. 2015, *ApJ*, 810, 25, doi: [10.1088/0004-637X/810/1/25](https://doi.org/10.1088/0004-637X/810/1/25)
- Grevesse, N., & Sauval, A. J. 1998, *SSRv*, 85, 161, doi: [10.1023/A:1005161325181](https://doi.org/10.1023/A:1005161325181)
- Groh, J. H., Ekström, S., Georgy, C., et al. 2019, *A&A*, 627, A24, doi: [10.1051/0004-6361/201833720](https://doi.org/10.1051/0004-6361/201833720)
- Gutkin, J., Charlot, S., & Bruzual, G. 2016, *MNRAS*, 462, 1757, doi: [10.1093/mnras/stw1716](https://doi.org/10.1093/mnras/stw1716)
- Harris, C. R., Millman, K. J., van der Walt, S. J., et al. 2020, *Nature*, 585, 357, doi: [10.1038/s41586-020-2649-2](https://doi.org/10.1038/s41586-020-2649-2)
- Heap, S. R., Lanz, T., & Hubeny, I. 2006, *ApJ*, 638, 409, doi: [10.1086/498635](https://doi.org/10.1086/498635)
- Hillier, D. J., & Miller, D. L. 1998, *ApJ*, 496, 407, doi: [10.1086/305350](https://doi.org/10.1086/305350)
- Howarth, I. D., & Prinja, R. K. 1989, *ApJS*, 69, 527, doi: [10.1086/191321](https://doi.org/10.1086/191321)
- Huang, W., & Gies, D. R. 2006, *ApJ*, 648, 580, doi: [10.1086/505782](https://doi.org/10.1086/505782)
- Hubeny, I., & Lanz, T. 1995, *ApJ*, 439, 875, doi: [10.1086/175226](https://doi.org/10.1086/175226)
- Hunter, J. D. 2007, *Computing In Science & Engineering*, 9, 90
- Izotov, Y. I., Orlová, I., Schaerer, D., et al. 2016, *Nature*, 529, 178, doi: [10.1038/nature16456](https://doi.org/10.1038/nature16456)
- Jacobs, B. A., Rizzi, L., Tully, R. B., et al. 2009, *AJ*, 138, 332, doi: [10.1088/0004-6256/138/2/332](https://doi.org/10.1088/0004-6256/138/2/332)
- Joye, W. A., & Mandel, E. 2003, in *Astronomical Society of the Pacific Conference Series*, Vol. 295, *Astronomical Data Analysis Software and Systems XII*, ed. H. E. Payne, R. I. Jedrzejewski, & R. N. Hook, 489
- Kehrig, C., Vílchez, J. M., Guerrero, M. A., et al. 2018, *MNRAS*, 480, 1081, doi: [10.1093/mnras/sty1920](https://doi.org/10.1093/mnras/sty1920)
- Krtićka, J., & Kubát, J. 2017, *A&A*, 606, A31, doi: [10.1051/0004-6361/201730723](https://doi.org/10.1051/0004-6361/201730723)
- Kudritzki, R.-P., & Puls, J. 2000, *ARA&A*, 38, 613, doi: [10.1146/annurev.astro.38.1.613](https://doi.org/10.1146/annurev.astro.38.1.613)
- Kunth, D., & Östlin, G. 2000, *A&A Rv*, 10, 1, doi: [10.1007/s001590000005](https://doi.org/10.1007/s001590000005)
- Lamers, H. J. G. L. M., & Cassinelli, J. P. 1999, *Introduction to Stellar Winds*
- Lamers, H. J. G. L. M., Snow, T. P., & Lindholm, D. M. 1995, *ApJ*, 455, 269, doi: [10.1086/176575](https://doi.org/10.1086/176575)
- Lanz, T., & Hubeny, I. 2003, *ApJS*, 146, 417, doi: [10.1086/374373](https://doi.org/10.1086/374373)
- Lee, H., Skillman, E. D., & Venn, K. A. 2005, *ApJ*, 620, 223, doi: [10.1086/427019](https://doi.org/10.1086/427019)
- Lee, H., Zucker, D. B., & Grebel, E. K. 2007, *MNRAS*, 376, 820, doi: [10.1111/j.1365-2966.2007.11481.x](https://doi.org/10.1111/j.1365-2966.2007.11481.x)
- Leitherer, C., Robert, C., & Drissen, L. 1992, *ApJ*, 401, 596, doi: [10.1086/172089](https://doi.org/10.1086/172089)
- Lejeune, T., & Schaerer, D. 2001, *A&A*, 366, 538, doi: [10.1051/0004-6361:20000214](https://doi.org/10.1051/0004-6361:20000214)
- Levesque, E. M., Leitherer, C., Ekstrom, S., Meynet, G., & Schaerer, D. 2012, *ApJ*, 751, 67, doi: [10.1088/0004-637X/751/1/67](https://doi.org/10.1088/0004-637X/751/1/67)
- Livermore, R. C., Finkelstein, S. L., & Lotz, J. M. 2017, *ApJ*, 835, 113, doi: [10.3847/1538-4357/835/2/113](https://doi.org/10.3847/1538-4357/835/2/113)
- Martins, F., & Palacios, A. 2021, *A&A*, 645, A67, doi: [10.1051/0004-6361/202039337](https://doi.org/10.1051/0004-6361/202039337)
- McQuinn, K. B. W., Skillman, E. D., Dolphin, A. E., & Mitchell, N. P. 2015a, *ApJ*, 808, 109, doi: [10.1088/0004-637X/808/2/109](https://doi.org/10.1088/0004-637X/808/2/109)
- McQuinn, K. B. W., Skillman, E. D., Dolphin, A., et al. 2015b, *ApJ*, 812, 158, doi: [10.1088/0004-637X/812/2/158](https://doi.org/10.1088/0004-637X/812/2/158)
- Meynet, G., & Maeder, A. 2002, *A&A*, 390, 561, doi: [10.1051/0004-6361:20020755](https://doi.org/10.1051/0004-6361:20020755)
- Mokiem, M. R., de Koter, A., Vink, J. S., et al. 2007, *A&A*, 473, 603, doi: [10.1051/0004-6361:20077545](https://doi.org/10.1051/0004-6361:20077545)

- Murphy, L. J., Groh, J. H., Farrell, E., et al. 2021, arXiv e-prints, arXiv:2105.06900.
<https://arxiv.org/abs/2105.06900>
- Naab, T., & Ostriker, J. P. 2017, *ARA&A*, 55, 59,
doi: [10.1146/annurev-astro-081913-040019](https://doi.org/10.1146/annurev-astro-081913-040019)
- Oesch, P. A., Bouwens, R. J., Illingworth, G. D., Labbé, I., & Stefanon, M. 2018, *ApJ*, 855, 105,
doi: [10.3847/1538-4357/aab03f](https://doi.org/10.3847/1538-4357/aab03f)
- Ouchi, M., Mobasher, B., Shimasaku, K., et al. 2009, *ApJ*, 706, 1136, doi: [10.1088/0004-637X/706/2/1136](https://doi.org/10.1088/0004-637X/706/2/1136)
- Penny, L. R., & Gies, D. R. 2009, *ApJ*, 700, 844,
doi: [10.1088/0004-637X/700/1/844](https://doi.org/10.1088/0004-637X/700/1/844)
- Perez, F., & Granger, B. E. 2007, *Computing in Science and Engineering*, 9, 21, doi: [10.1109/MCSE.2007.53](https://doi.org/10.1109/MCSE.2007.53)
- Przybill, N., Firnstein, M., Nieva, M. F., Meynet, G., & Maeder, A. 2010, *A&A*, 517, A38,
doi: [10.1051/0004-6361/201014164](https://doi.org/10.1051/0004-6361/201014164)
- Ramachandran, V., Oskinova, L. M., & Hamann, W. R. 2021, *A&A*, 646, A16, doi: [10.1051/0004-6361/202039486](https://doi.org/10.1051/0004-6361/202039486)
- Ramachandran, V., Hamann, W. R., Oskinova, L. M., et al. 2019, *A&A*, 625, A104,
doi: [10.1051/0004-6361/201935365](https://doi.org/10.1051/0004-6361/201935365)
- Ramírez-Agudelo, O. H., Simón-Díaz, S., Sana, H., et al. 2013, *A&A*, 560, A29, doi: [10.1051/0004-6361/201321986](https://doi.org/10.1051/0004-6361/201321986)
- Robertson, B. E., Ellis, R. S., Furlanetto, S. R., & Dunlop, J. S. 2015, *ApJL*, 802, L19,
doi: [10.1088/2041-8205/802/2/L19](https://doi.org/10.1088/2041-8205/802/2/L19)
- Schaerer, D., & de Koter, A. 1997, *A&A*, 322, 598.
<https://arxiv.org/abs/astro-ph/9611068>
- Senchyna, P., Stark, D. P., Charlot, S., et al. 2021, *MNRAS*, 503, 6112, doi: [10.1093/mnras/stab884](https://doi.org/10.1093/mnras/stab884)
- Senchyna, P., Stark, D. P., Chevallard, J., et al. 2019, *MNRAS*, 488, 3492, doi: [10.1093/mnras/stz1907](https://doi.org/10.1093/mnras/stz1907)
- Simón-Díaz, S., & Herrero, A. 2014, *A&A*, 562, A135,
doi: [10.1051/0004-6361/201322758](https://doi.org/10.1051/0004-6361/201322758)
- Skillman, E. D., Kennicutt, R. C., & Hodge, P. W. 1989, *ApJ*, 347, 875, doi: [10.1086/168178](https://doi.org/10.1086/168178)
- Skillman, E. D., Salzer, J. J., Berg, D. A., et al. 2013, *AJ*, 146, 3, doi: [10.1088/0004-6256/146/1/3](https://doi.org/10.1088/0004-6256/146/1/3)
- Smith, N. 2014, *ARA&A*, 52, 487,
doi: [10.1146/annurev-astro-081913-040025](https://doi.org/10.1146/annurev-astro-081913-040025)
- Somerville, R. S., & Davé, R. 2015, *ARA&A*, 53, 51,
doi: [10.1146/annurev-astro-082812-140951](https://doi.org/10.1146/annurev-astro-082812-140951)
- Steidel, C. C., Bogosavljević, M., Shapley, A. E., et al. 2018, *ApJ*, 869, 123, doi: [10.3847/1538-4357/aaed28](https://doi.org/10.3847/1538-4357/aaed28)
- Szécsi, D., Langer, N., Yoon, S.-C., et al. 2015, *A&A*, 581, A15, doi: [10.1051/0004-6361/201526617](https://doi.org/10.1051/0004-6361/201526617)
- The HDF Group. 1997-2020
- Tinsley, B. M. 1980, *FCPh*, 5, 287
- Topping, M. W., & Shull, J. M. 2015, *ApJ*, 800, 97,
doi: [10.1088/0004-637X/800/2/97](https://doi.org/10.1088/0004-637X/800/2/97)
- Tramper, F., Sana, H., de Koter, A., & Kaper, L. 2011, *ApJL*, 741, L8, doi: [10.1088/2041-8205/741/1/L8](https://doi.org/10.1088/2041-8205/741/1/L8)
- Tramper, F., Sana, H., de Koter, A., Kaper, L., & Ramírez-Agudelo, O. H. 2014, *A&A*, 572, A36,
doi: [10.1051/0004-6361/201424312](https://doi.org/10.1051/0004-6361/201424312)
- Trebitch, M., Blaizot, J., Rosdahl, J., Devriendt, J., & Slyz, A. 2017, *MNRAS*, 470, 224,
doi: [10.1093/mnras/stx1060](https://doi.org/10.1093/mnras/stx1060)
- Vink, J. S., de Koter, A., & Lamers, H. J. G. L. M. 2001, *A&A*, 369, 574, doi: [10.1051/0004-6361:20010127](https://doi.org/10.1051/0004-6361:20010127)
- Vink, J. S., & Sander, A. A. C. 2021, *MNRAS*, 504, 2051,
doi: [10.1093/mnras/stab902](https://doi.org/10.1093/mnras/stab902)
- Virtanen, P., Gommers, R., Oliphant, T. E., et al. 2020, *Nature Methods*, 17, 261, doi: [10.1038/s41592-019-0686-2](https://doi.org/10.1038/s41592-019-0686-2)
- Walborn, N. R., & Fitzpatrick, E. L. 1990, *PASP*, 102, 379,
doi: [10.1086/132646](https://doi.org/10.1086/132646)
- Williams, B. F., Lang, D., Dalcanton, J. J., et al. 2014, *ApJS*, 215, 9, doi: [10.1088/0067-0049/215/1/9](https://doi.org/10.1088/0067-0049/215/1/9)
- Williams, B. F., Durbin, M. J., Dalcanton, J. J., et al. 2021, *ApJS*, 253, 53, doi: [10.3847/1538-4365/abdf4e](https://doi.org/10.3847/1538-4365/abdf4e)
- Wise, J. H., & Cen, R. 2009, *ApJ*, 693, 984,
doi: [10.1088/0004-637X/693/1/984](https://doi.org/10.1088/0004-637X/693/1/984)